

# Extraction of Single and Double Differential Cross-Sections on Argon for CC1 $\mu$ 2p0 $\pi$ Event Topologies in the SBND

Emilio Peláez Cisneros

July 22, 2024

## Abstract

The precise measurement of cross-sections for a variety of interactions is critical to the success of upcoming flagship neutrino experiments. Of special interest are neutrino interactions that leave the nucleus in a 2-particle 2-hole state (2p2h). This note will present cross-section measurements for the production of 2p2h states on Argon. Using SBND data collected from the **period** of operation, we select events corresponding to a charged-current  $\nu_\mu$  interaction that left the Argon nucleus in a 2p2h state. These interactions produce a topology with one muon and two protons in the final state (CC1 $\mu$ 2p0 $\pi$ ). This analysis targets both single differential and double differential cross-section measurements for CC1 $\mu$ 2p0 $\pi$  event topologies in a variety of kinematic variables. Comparisons are made to a set of theoretical models that explore different cross-section modeling configurations. Code for this analysis is available on [GitHub](#).

## Contents

<b>1</b>	<b>Introduction and motivation</b>	<b>2</b>
<b>2</b>	<b>Generator analysis</b>	<b>2</b>
2.1	Signal definition	2
2.2	Generators	2
2.3	Variables definition	3
2.4	Pre-FSI events	3
2.5	Double differential plots	9
2.6	Pure MEC events	9
<b>3</b>	<b>SBND analysis</b>	<b>15</b>
3.1	Fiducial volume	15
3.2	Signal definition	15
3.3	Variable plots	16
3.4	Signal efficiency	16
3.5	Migration and response matrices	16
3.6	Systematics	18
<b>4</b>	<b>Closure test</b>	<b>29</b>
<b>5</b>	<b>Cross-section results</b>	<b>29</b>
<b>6</b>	<b>Appendices</b>	<b>32</b>
6.1	Cross section systematics	32
<b>7</b>	<b>References</b>	<b>45</b>

# 1 Introduction and motivation

2 Since many current and next generation neutrino oscillation experiments will utilize dense nuclear targets,  
3 such as liquid argon (LAr), it is critical to characterize the impact of nuclear effects on neutrino cross-sections.  
4 One area of interest are neutrino events that eject 2 nucleons from the nucleus, leaving it with 2 holes: known  
5 as 2-particle 2-hole states (2p2h). The general picture is that the neutrino has a charged-current interaction  
6 with a neutron in the nucleus, producing a proton with significant momentum; this proton interacts with  
7 another proton, producing the 2p2h state. While the majority of 2p2h states are caused by Meson Exchange  
8 Currents (MEC) [15], some nuclear effects, such as Short-Range Nucleon-Nucleon correlations (SRC) [10],  
9 can also produce these states. In an accelerator-based liquid argon time projection chamber (LArTPC)  
10 experiment, such as SBND, a charged-current (CC) muon neutrino ( $\nu_\mu$ ) interaction that results in a 2p2h  
11 state would have a final state topology of 1 muon, 2 protons, and no charged or neutral pions. While  
12 there are existing measurements of CC1 $\mu$ 2p0 $\pi$  events on argon, the analyses were statistically limited and  
13 no cross-sections were extracted [1, 19]. There was a previous report with single differential cross-section  
14 measurements from the MicroBooNE detector [20], but this document presents the first double differential  
15 cross-section measurements of CC1 $\mu$ 2p0 $\pi$  topologies on argon, using data collected from the period of SBND  
16 operations.

## 17 2 Generator analysis

### 18 2.1 Signal definition

19 We choose charged-current muon neutrino interactions that result in one muon, two protons, no charged pions  
20 with  $P_\pi > 70$  MeV/c, no neutral pions or heavier mesons, and any number of neutrons. These interactions  
21 are denoted as CC1 $\mu$ 2p0 $\pi$ . We require the momentum of the muon and protons to be in the following ranges  
22 (in MeV/c):

$$100 < P_P < 1200 \quad 300 < P_\mu < 1000 \quad (1)$$

### 23 2.2 Generators

24 The following generators are used to create events, which are then discriminated using the signal definition  
25 above: NuWro, GiBUU, NEUT, GENIE G18, GENIE AR23. Information about these generators is  
26 summarized in Table 1.

Name	Generator/Configuration
G18	GENIE v3.0.6 G18_10a_02_11a
AR23	G18 with SuSAv2 MEC model
NuWro	NuWro 19.02.1
NEUT	NEUT v5.4.0
GiBUU	GiBUU 2021

Table 1: Generator and configuration data.

27 The GENIE configurations we used are:

- 28 (i) GENIE G18 [2, 3]: This modern model configuration uses the local Fermi gas (LFG) model [9],  
29 the Nieves CCQE scattering prescription [23], which includes Coulomb corrections for the outgoing  
30 muon [11], and random phase approximation (RPA) corrections [22]. Additionally, it uses the  
31 Nieves MEC model [25], the KuzminLyubushkin-Naumov Berger-Sehgal RES [6, 27, 16], Berger-Sehgal  
32 COH [7] and Bodek-Yang DIS [28] scattering models with the PYTHIA [26] hadronization part, and  
33 the hA2018 FSI model [4].
- 34 (ii) GENIE AR23: Same as the G18 model configuration but using the SuSAv2 MEC model.

35 The alternative event generators are:

- 36 (i) NuWro [12]: Includes the LFG model [9], the Llewellyn Smith model for QE events [18], the Nieves  
37 model for MEC events [24], the AdlerRarita-Schwinger formalism to calculate the  $\Delta$  resonance explicitly [13],  
38 the Berger-Sehgal (BS) COH [7] scattering model, an intranuclear cascade model for FSI [24],  
39 and a coupling to PYTHIA [26] for hadronization.
- 40 (ii) NEUT [14]: Corresponds to the combination of the LFG model [8, 9], the Nieves CCQE scattering  
41 prescription [23], the Nieves MEC model using a lookup table [25], the Berger Sehgal RES [6, 13, 5]  
42 and BS COH [7] scattering models, FSI with medium corrections for pions [2, 3], and PYTHIA [26]  
43 purposes.
- 44 (iii) GiBUU [21]: Uses similar models to GENIE, but they are implemented in a coherent way by solving  
45 the Boltzmann-Uehling-Uhlenbeck transport equation [21]. The modeling includes the LFG model [9],  
46 a standard CCQE expression [17], an empirical MEC model, and a dedicated spin dependent resonance  
47 amplitude calculation following the MAID analysis [21]. The DIS model is from PYTHIA [26]. GiBUU's  
48 FSI treatment propagates the hadrons through the residual nucleus in a nuclear potential consistent  
49 with the initial state.

### 50 2.3 Variables definition

51 Given the momentum vectors for the leading proton  $\vec{p}_L$ , recoil proton  $\vec{p}_R$ , and muon  $\vec{p}_\mu$ , we define several  
52 variables. First, we define the momenta and opening angle of each variable, denoted as  $|\vec{p}|$  and  $\cos(\theta_{\vec{p}})$ , with  
53 the appropriate index for each momentum vector. These variables are plotted in Figure 1.

54 We also define variables relating the multiple momentum vectors. First, the opening angle between the  
55 protons in the lab frame, given by

$$\cos(\theta_{\vec{p}_L, \vec{p}_R}) = \frac{\vec{p}_L \cdot \vec{p}_R}{|\vec{p}_L| |\vec{p}_R|}. \quad (2)$$

56 Then, the opening angle between the total proton momentum ( $\vec{p}_{\text{sum}} = \vec{p}_L + \vec{p}_R$ ) and the muon, given by

$$\cos(\theta_{\vec{p}_\mu, \vec{p}_{\text{sum}}}) = \frac{\vec{p}_\mu \cdot \vec{p}_{\text{sum}}}{|\vec{p}_\mu| |\vec{p}_{\text{sum}}|}. \quad (3)$$

57 The momentum transverse to the direction of the neutrino beam, which we denote  $\delta\vec{P}_T$  and is given by

$$\delta\vec{P}_T = \vec{p}_T^\mu + \vec{p}_T^L + \vec{p}_T^R. \quad (4)$$

58 For the transverse momentum, we will be interested in its magnitude  $|\delta\vec{P}_T|$ . Finally, the angular orientation  
59 of the transverse momentum with respect to the transverse muon is defined as

$$\delta\alpha_T = \cos^{-1} \left( \frac{-\vec{p}_T^\mu \cdot \delta\vec{P}_T}{|\vec{p}_T^\mu| |\delta\vec{P}_T|} \right). \quad (5)$$

60 We plot the differential cross sections of these variables for the given generators in Figure 2. We can also  
61 see the cross section by event type for  $|\delta\vec{P}_T|$  for the all generators in Figure 3. We only show one variable  
62 for the interaction breakdown, as the percentages will remain the same for other variables.

### 63 2.4 Pre-FSI events

64 To investigate why the percentage of MEC events for some generators is low, we performed event selection  
65 before any final state interactions took place. For both GENIE tunes, NEUT, and NuWro, we got 100%  
66 MEC events pre-FSI. For GiBUU, only 4.1% MEC versus 76.2% RES and 16% DIS events pre-FSI. The  
67 interaction breakdown plots for all the generators are shown in Figure 4. Again, only one variable is shown  
68 as the percentages will remain the same for others. Since GiBUU is the outlier, we checked the specific  
69 interaction mode for the resonance events. We got that 10 has 39.3%, 11 has 34.7%, 12 has 0.0136%, 13 has  
70 26 %, and 27, 22, and 23 all have zero percent of the resonance events. We also checked the event interaction  
71 breakdown for GiBUU samples without final state interactions, in which we found that 100% of the events  
72 are MEC, shown in Figure 5.

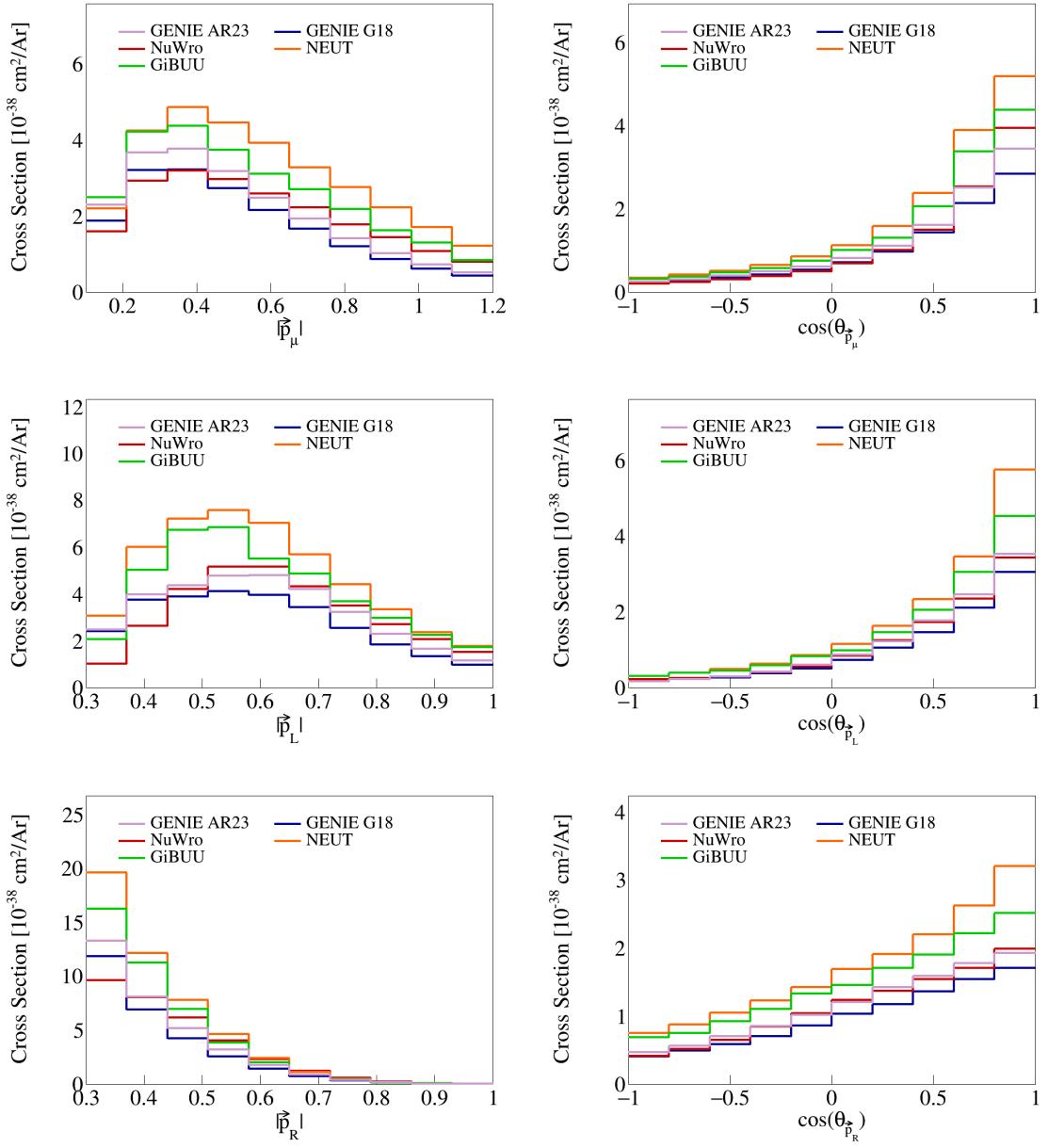


Figure 1: Cross sections for momentum and opening angles of individual particles.

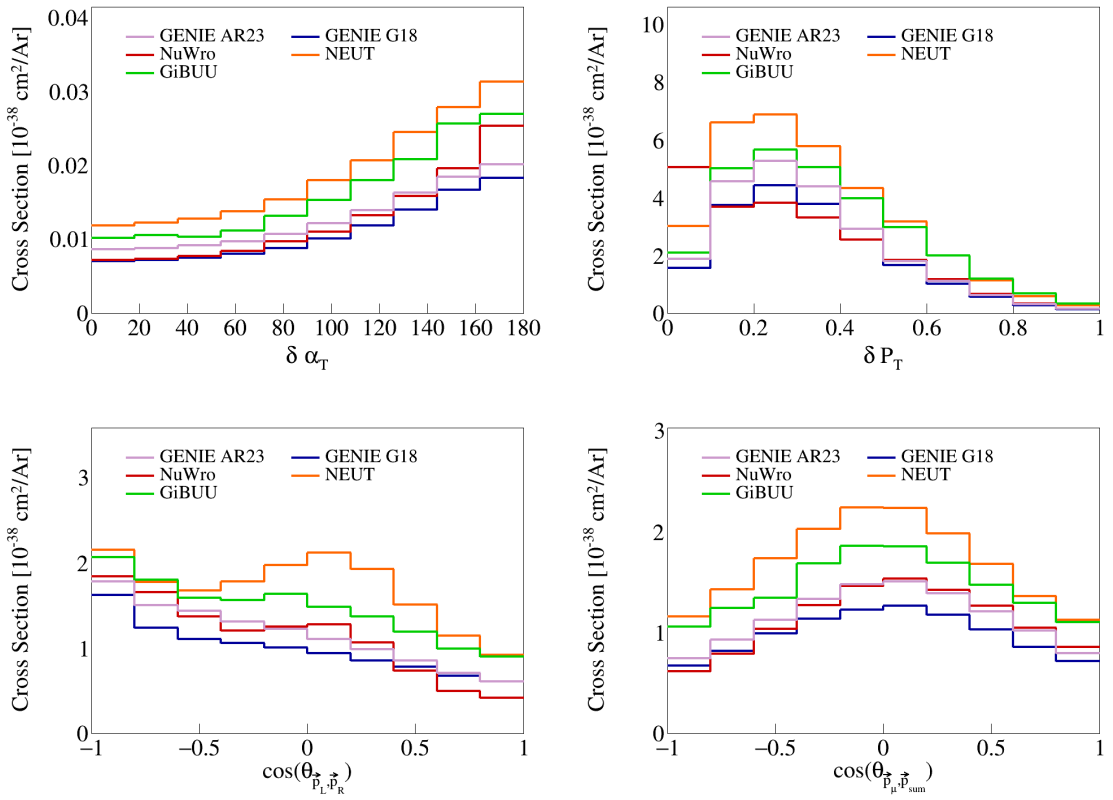


Figure 2: Cross sections for opening angles and transverse momentum.

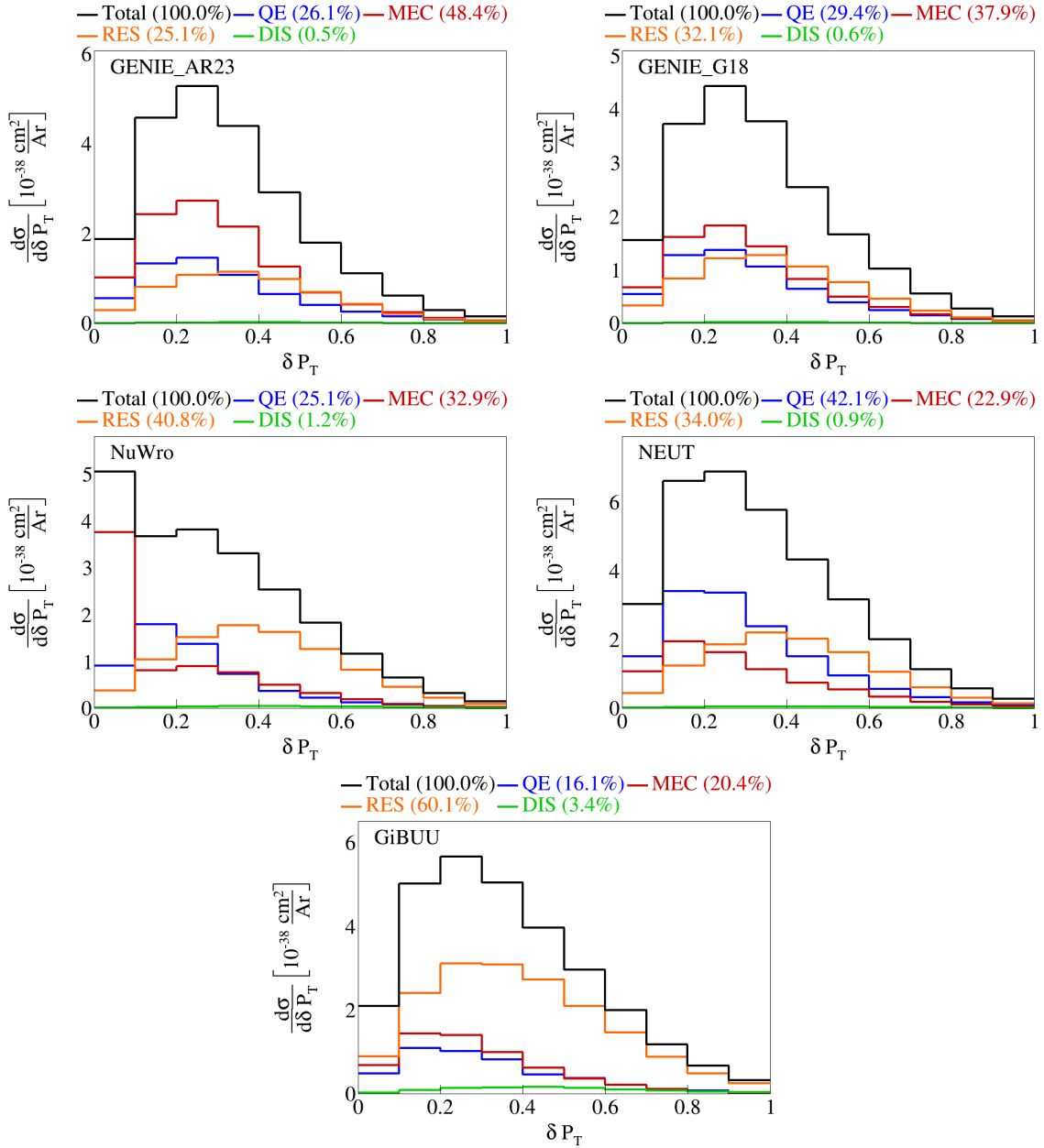


Figure 3: Event interaction breakdown for  $|\delta \vec{P}_T|$ .

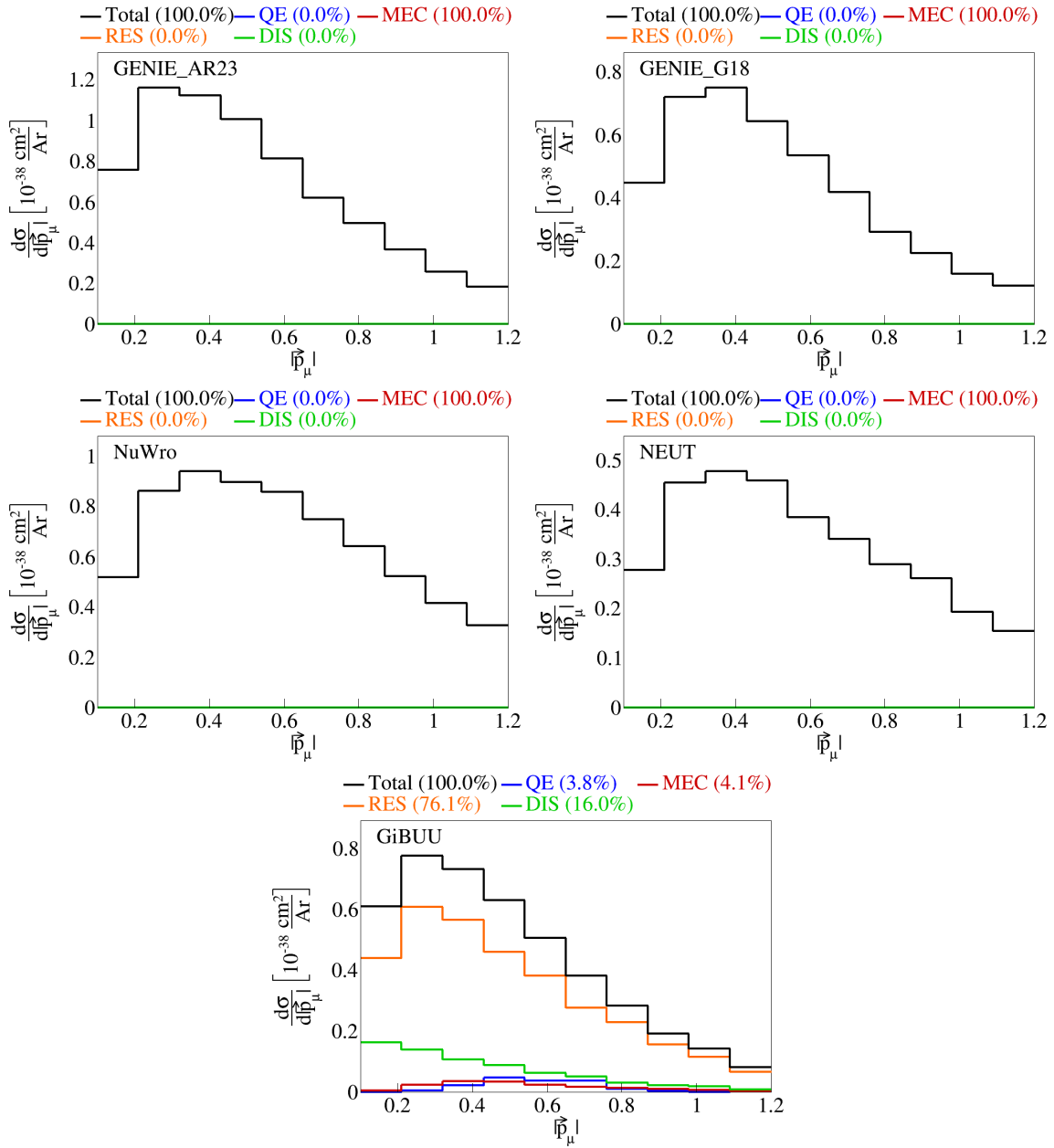


Figure 4: Event interaction breakdown of  $|\vec{p}_\mu|$  before final state interactions.

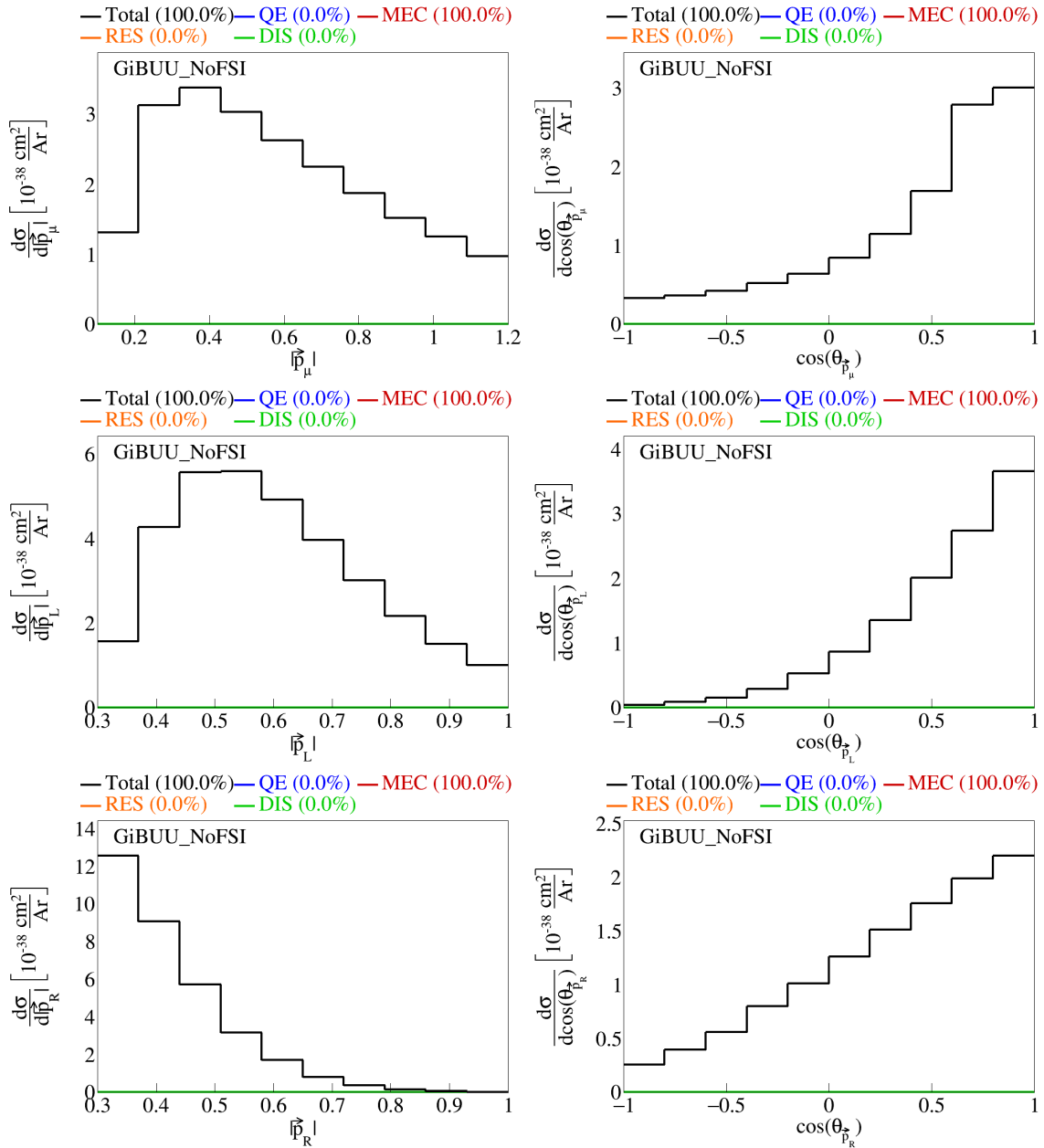


Figure 5: Event interaction breakdown for final events from GiBUU events with no FSI.

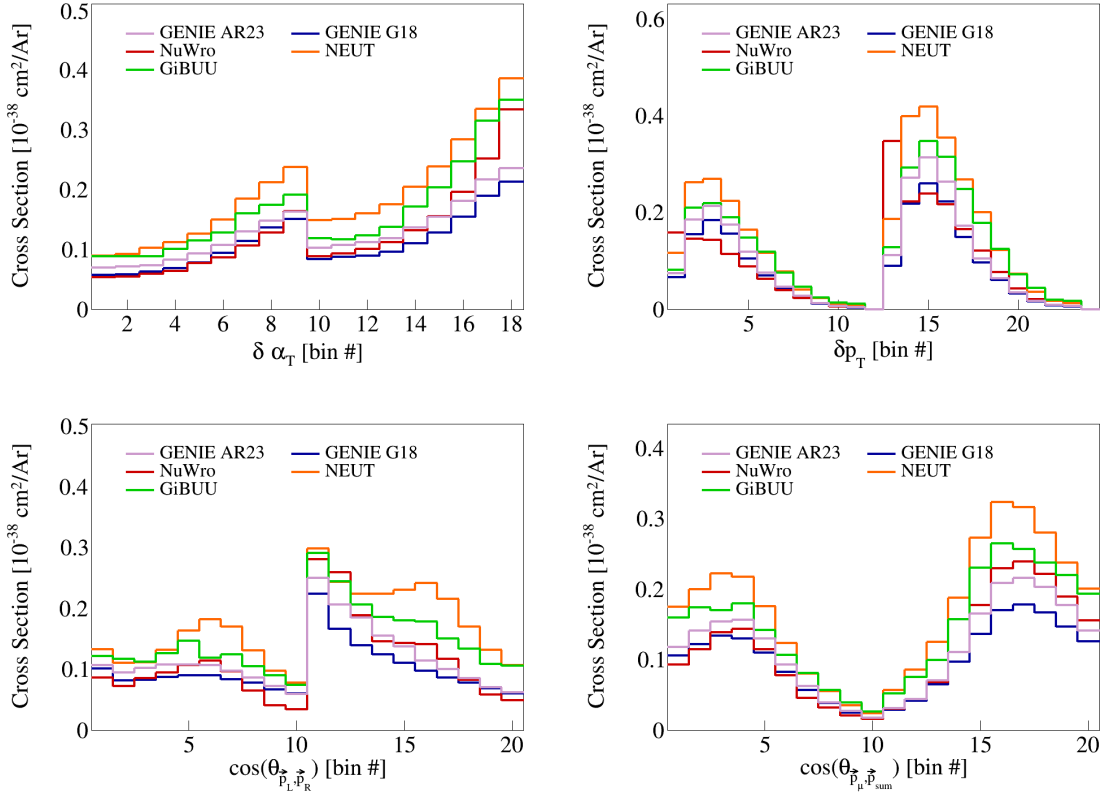


Figure 6: Double differential serial plots, all in  $\cos(\theta_{\vec{p}_\mu})$ .

## 2.5 Double differential plots

For our double differential figures, we plot  $\delta P_T$ ,  $\delta \alpha_T$ ,  $\cos(\theta_{\vec{p}_L, \vec{p}_R})$ , and  $\cos(\theta_{\vec{p}_\mu, \vec{p}_{\text{sum}}})$  in  $\cos(\theta_{\vec{p}_\mu})$ . These are shown in Figure 6. We have two bins for  $\cos(\theta_{\vec{p}_\mu})$ , the first one going from  $-1$  to  $0.5$  and the second from  $0.5$  to  $1$ . Therefore, these are irregular bins, with the first holding a larger range than the second. The interaction breakdown for  $\delta \alpha_T$  in  $\cos(\theta_{\vec{p}_\mu})$  is shown in Figure 7.

We also slice the double differential plots into two plots each, so that we have  $\cos(\theta_{\vec{p}_\mu})$  in the horizontal axis instead of bin numbers. These plots are shown in Figure 8. In these plots, the bins contents have been reweighted appropriately, by dividing the content of each bin by the width of the bin for the variable in the axis multiplied by the width of the  $\cos(\theta_{\vec{p}_\mu})$  slice. Note that the plots for the  $0.5 < \cos(\theta_{\vec{p}_\mu}) < 1$  slice have more events in general, although they span a smaller phase space of  $\cos(\theta_{\vec{p}_\mu})$ , as it can be seen by the scale of the vertical axis. We performed the same double differential analysis for the events before final state interactions. These are shown in Figure 9.

## 2.6 Pure MEC events

We also generated pure MEC events with different configurations to get the MEC splines. These were all different tunes of GENIE: AR23, G18 with Empirical MEC model, and G18 with Nieves MEC model. The plots for the transverse kinematic variables are shown in Figure 10. The sliced double differential plots are shown in Figure 11.

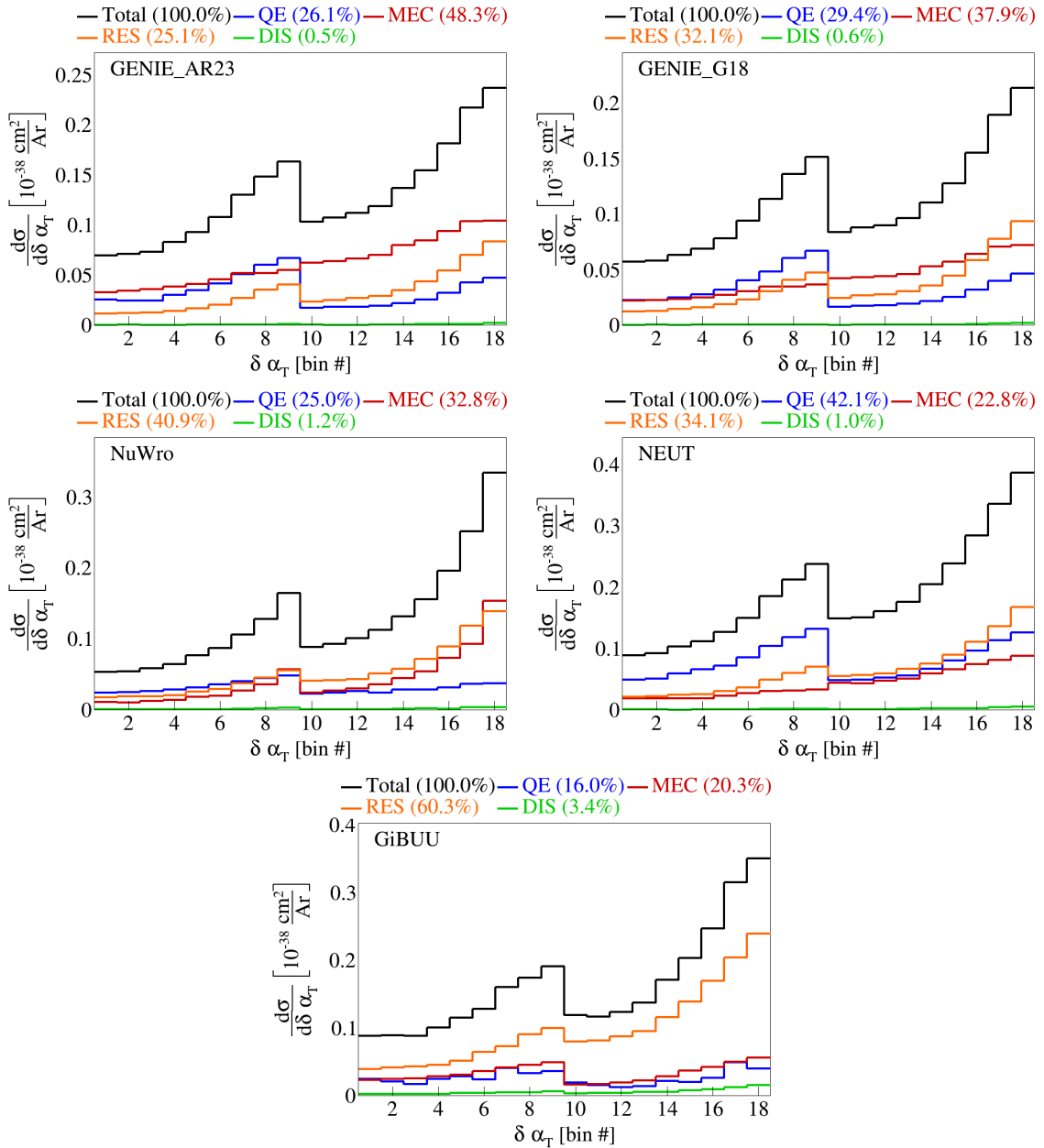


Figure 7: Interaction breakdown for  $\delta\alpha_T$  in  $\cos(\theta_{\vec{p}_\mu})$ .

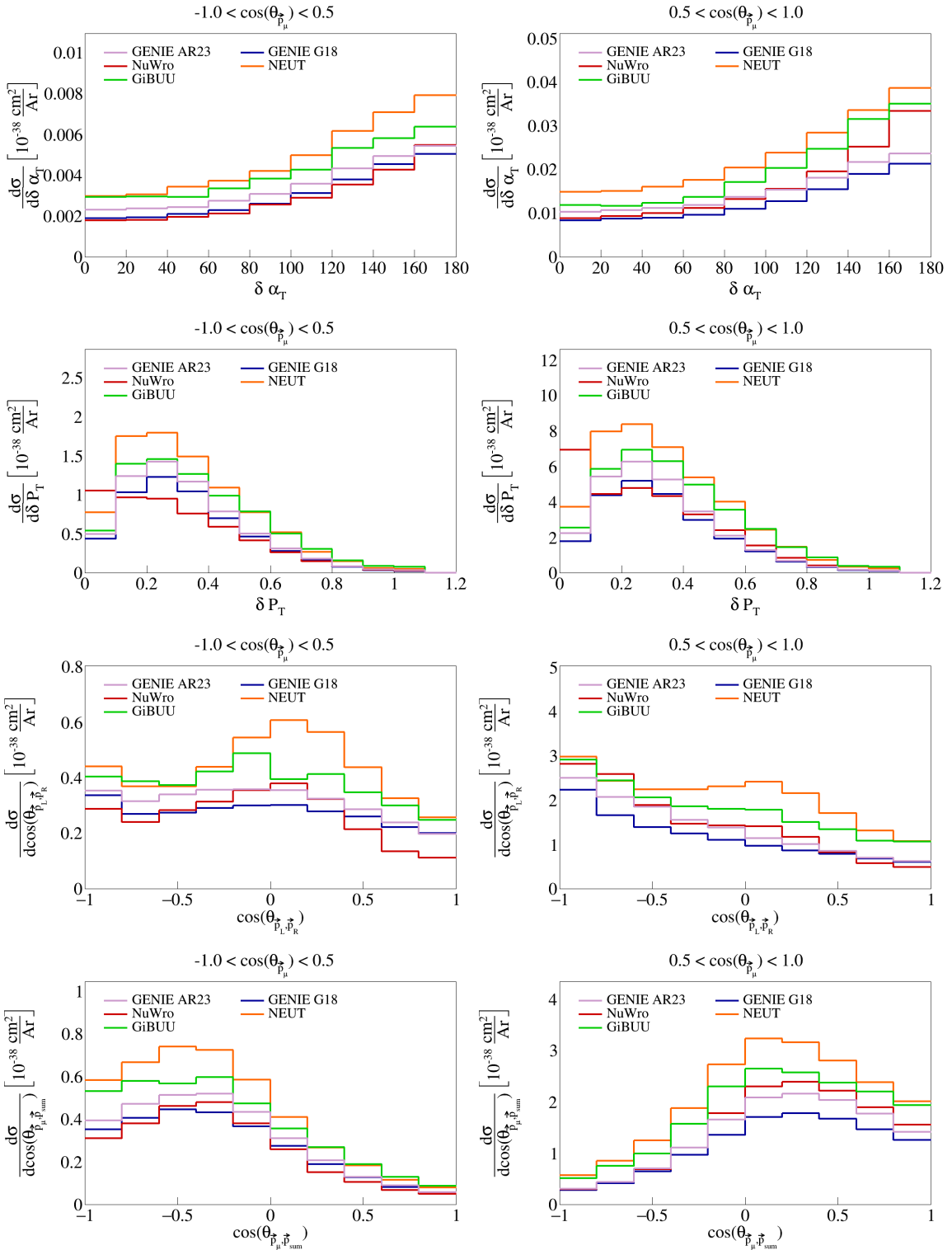


Figure 8: Sliced double differential plots.

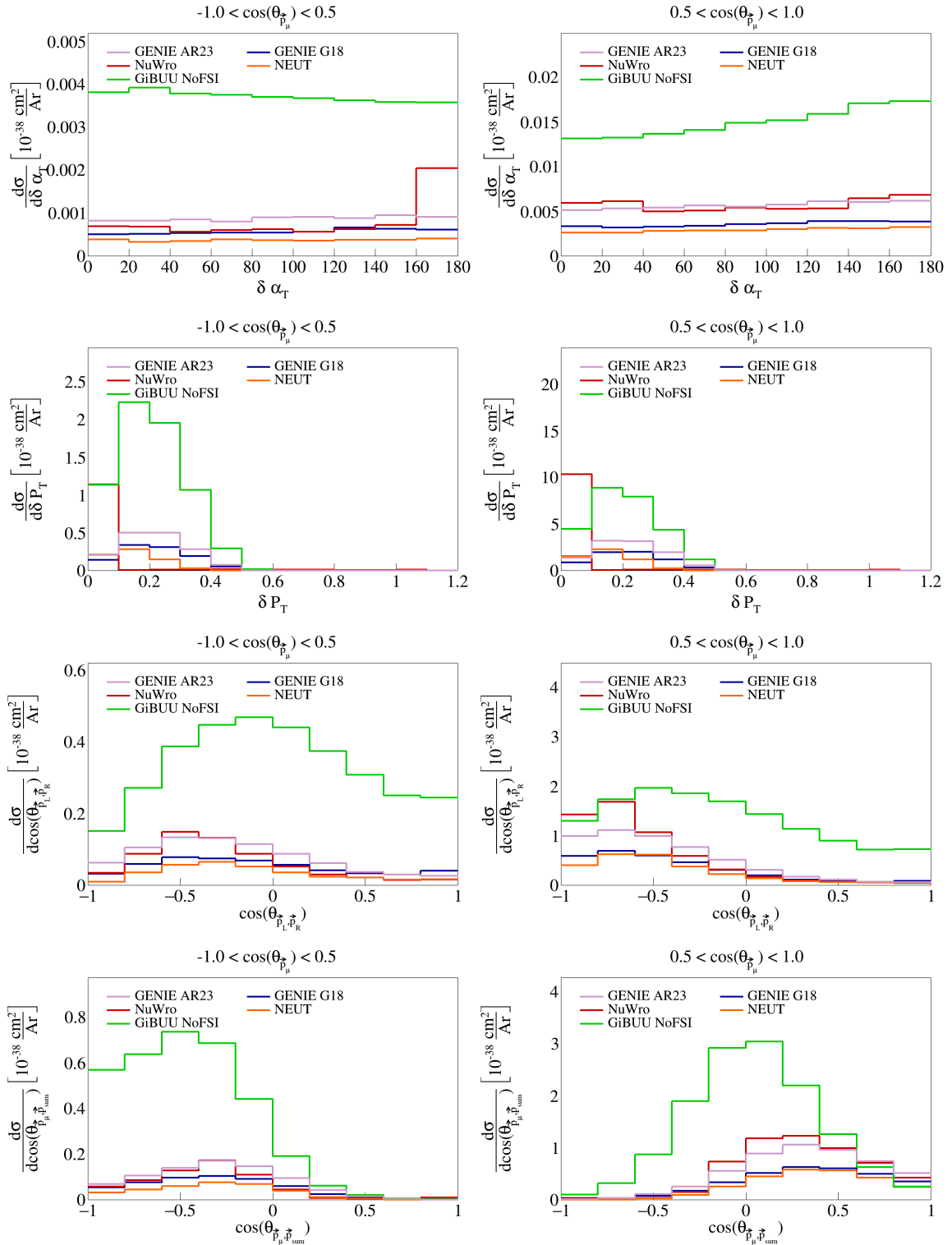


Figure 9: Sliced double differential plots for pre-FSI events.

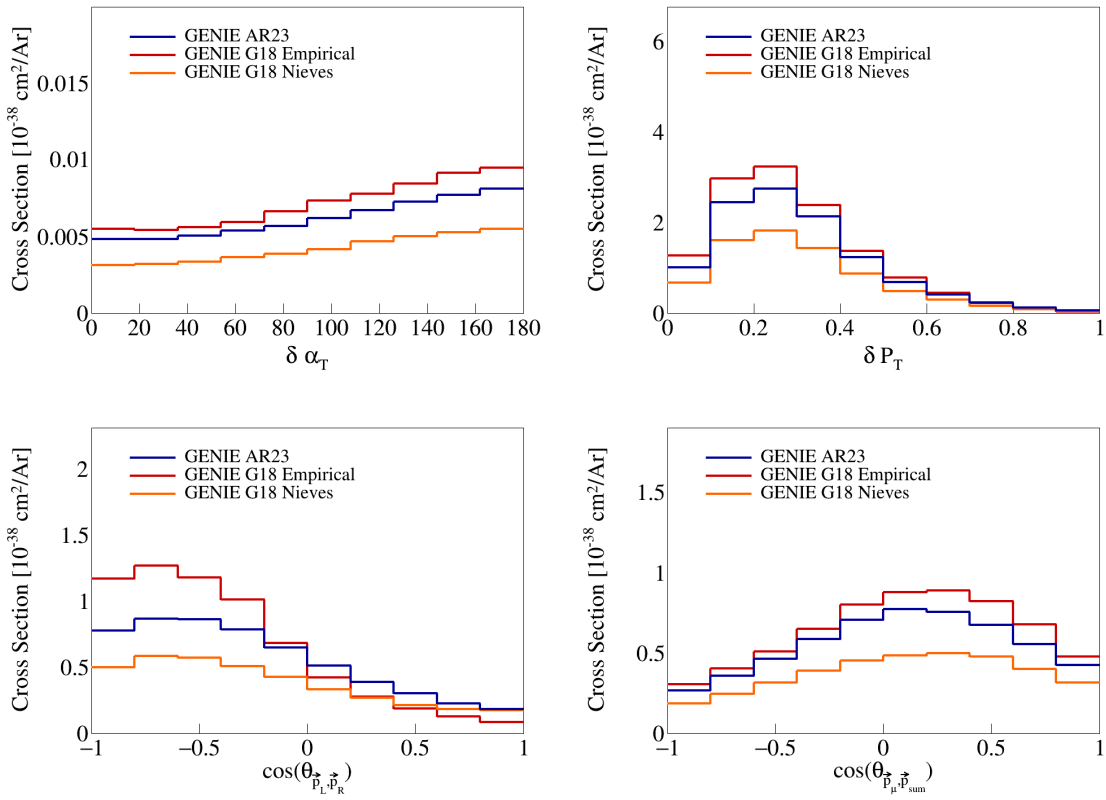


Figure 10: Transverse kinematic variables for pure MEC events.

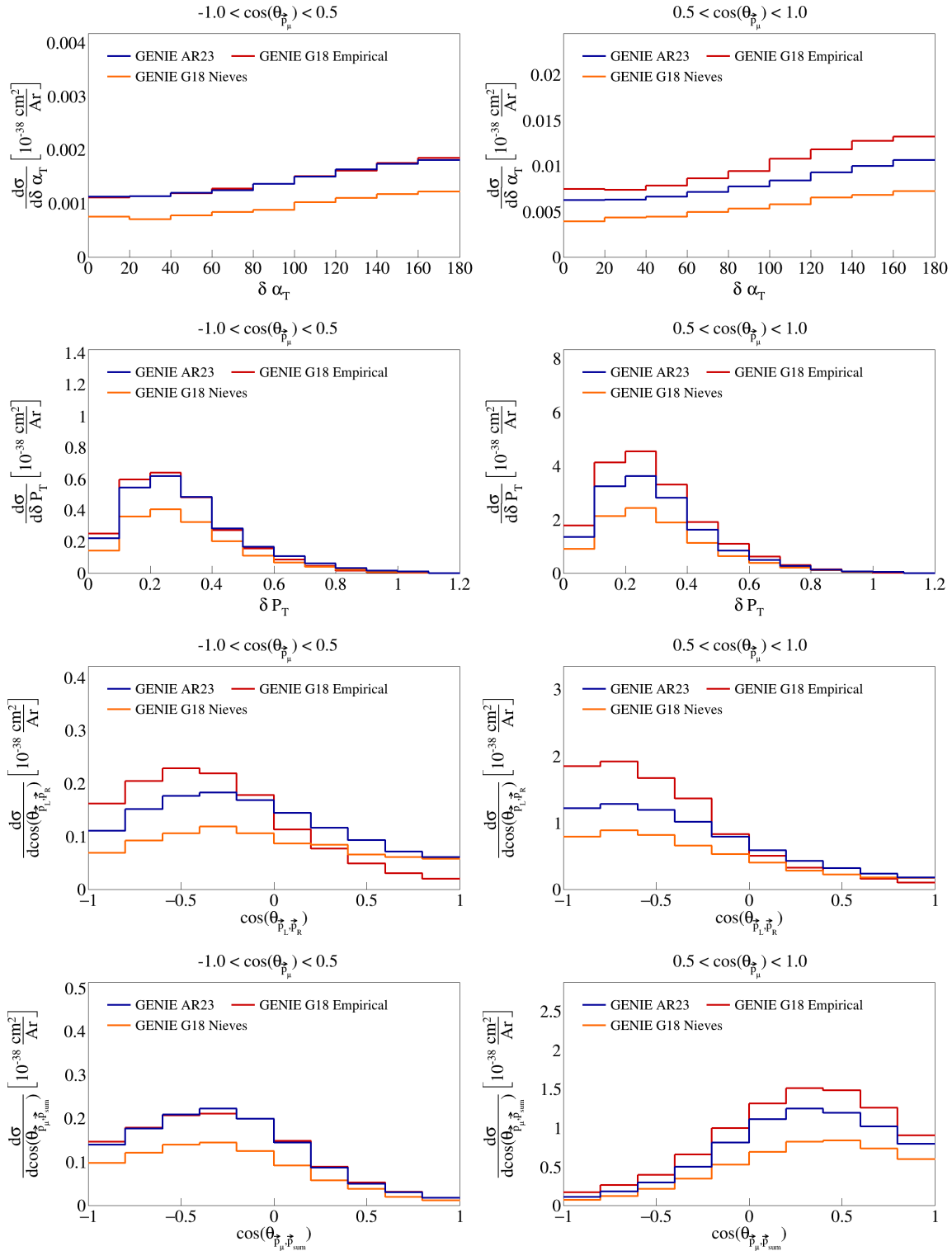


Figure 11: Sliced double differential plots for pure MEC events.

## 90 3 SBND analysis

91 The CAF files used for this analysis are available in the Fermilab gpvms at the path

92 `/pnfs/sbnd/persistent/users/apapadop/CAF_Files/*.flat.caf.root`

93 where the asterisk means that all the files in the directory with the extension `.flat.caf.root` will be used.

### 94 3.1 Fiducial volume

95 To perform the analysis of SBND data, we have to define the fiducial volume of the detector, which represents  
96 a central part of the detector in which we will accept signals. The fiducial volume is given by the following  
97 ranges:

$$5 < |x| < 180 \quad |y| < 180 \quad 10 < z < 450 \quad (6)$$

98 where  $x$ ,  $y$ , and  $z$  are the coordinates in the detector frame, all in centimeters.

### 99 3.2 Signal definition

100 To perform analysis on experiment data, we will be using the CAFAna framework. This allows us to perform  
101 cuts based on the reconstructed and Monte Carlo data (if available, i.e., only in the case of dealing with  
102 simulated events), to discriminate events. To discriminate events based on their Monte Carlo data, we  
103 perform a simple `TruthCut` that checks the following:

- 104 (i) That the neutrino interaction takes place in the fiducial volume.
- 105 (ii) That the neutrino is a muon neutrino.
- 106 (iii) That the interaction is a charged current interaction.
- 107 (iv) That there is only one muon in our allowed momentum range.
- 108 (v) That there are only two protons in our allowed momentum range.
- 109 (vi) That there are no charged/neutral pions in our defined momenta ranges.

110 Using the reconstructed event data, the cut we have to use is not as simple as in the Monte Carlo data  
111 case. We now have to use a `Cut` that looks at different variables of the reconstructed event to determine if  
112 it is a signal event. We perform the following cuts:

- 113 (i) Cosmic: that the event is not a cosmic event by Pandora's criteria, i.e., requiring `nu_score > 0.4` to  
114 check how neutrino-like the event is, and `fmatch.score < 7` with  $0 < fmatch.time < 1.8$  to check the  
115 event comes from the beam.
- 116 (ii) Vertex in FV: that the reconstructed vertex for the neutrino interaction takes place in the fiducial  
117 volume defined above.
- 118 (iii) One muon: that there is one muon track with  $L_{\text{track}} > 50$  cm, starting point in the fiducial volume,  
119  $\chi^2_\mu < 30$ ,  $\chi^2_p > 60$ , with momentum in our allowed range; if there are multiple candidate tracks, the  
120 one with the longest track length is chosen.
- 121 (iv) Two protons: that there are two proton tracks with  $\chi^2_p < 100$ , full track in the fiducial volume, and  
122 that these have momentum in our allowed range.
- 123 (v) No charged pions: that there are no other reconstructed tracks with momentum in the allowed range  
124 for charged pions inside the fiducial volume.
- 125 (vi) No neutral pions: that there are no reconstructed particles with a positive `trackScore` less than 0.5  
126 indicating a shower, so we don't allow any neutral pions.

Cut	Number of events	Global efficiency	Signal efficiency	Purity
All	1.31823e7	-	-	-
True signal events	273751	-	-	-
All reco events	6.61683e6	100%	-	-
Cosmic cut	5.46987e6	82.6659%	89.0567%	4.45703%
Vertex in FV cut	3.10952e6	46.9941%	87.5899%	7.7111%
One muon cut	2.14513e06	32.4193%	69.629%	8.88571%
Two protons cut	137309	2.07514%	16.3503%	32.5975%
No charged pions cut	65938	0.99652%	12.1369%	50.3881%
No neutral pions cut	54088.9	0.817444%	10.929%	55.313%

Table 2: Global efficiency, selection efficiency, and purity for cuts made in signal definition.

127 Using these two discriminators on simulated events, the reconstructed events that satisfy the signal definition,  
 128 and distinguish between true signal events and background events.

129 We use a one-bin histogram with lower bound 0 and upper bound of 3 in the true energy variable to get  
 130 total counts of generated events, true signal events, all reconstructed events, and efficiency and purity data  
 131 after each of the cuts described above is applied to the reconstructed events. These results are shown in  
 132 Table 2. Counts are obtained using ROOT’s command `Histo->Integral()`. Global efficiency is defined as  
 133 the ratio between events that pass the cut and reconstructed events, signal efficiency as the ratio between  
 134 true events that pass the cut and the all true signal events, and purity as the ratio between true signal events  
 135 that pass the cut and all events that pass the cut. The numbers reported in this table are POT normalized  
 136 to  $6.6 \times 10^{20}$ .

### 137 3.3 Variable plots

138 Using all the variable definitions as we did when studying the event generators, and the signal definition  
 139 based on the cuts described in the previous section, we can generate plots for SBND data. The reconstructed  
 140 single differential variables corresponding to vector opening angles and magnitudes are shown in Figure 12.  
 141 In these figures, three lines are shown, corresponding to: all reconstructed (all the reconstructed events that  
 142 pass our signal definition), signal (reconstructed events that pass signal definition and are true signal events  
 143 as determined by the `TruthCut` from our previous section), and background (reconstructed events that pass  
 144 signal definition but are not true signal events) events. Similarly, the variables relating multiple vectors are  
 145 shown in Figure 13, and double differential sliced variables are shown in Figure 14.

### 146 3.4 Signal efficiency

147 Using the truth information about reconstructed events, we can also compute signal efficiency on a bin-by-  
 148 bin basis. To be precise, signal definition on a bin *i* is defined as the ratio between the number of events  
 149 generated in bin *i* and reconstructed in any bin over the number of events generated in bin *i*. These plots  
 150 are shown in Figure 15 and Figure 16 for single-differential variables and Figure 17 for double differential  
 151 variables.

### 152 3.5 Migration and response matrices

153 Further, we compute migration matrices which give us a measure of how reliable our reconstructed variables  
 154 are. A given column in this matrix represents a bin of the truth variable, i.e., the value with which the  
 155 event was generated. Then, each row corresponds to a reconstructed bin of the same variable, and each cell  
 156 corresponds to the probability that an event generated with the truth value corresponding to the column gets  
 157 reconstructed with the value corresponding to the row. For the migration matrix, we consider true signal  
 158 events that were reconstructed and satisfy our signal definition in the denominator. Therefore, the values in  
 159 each column must add up to 1. The migration matrices for the single differential variables are presented in

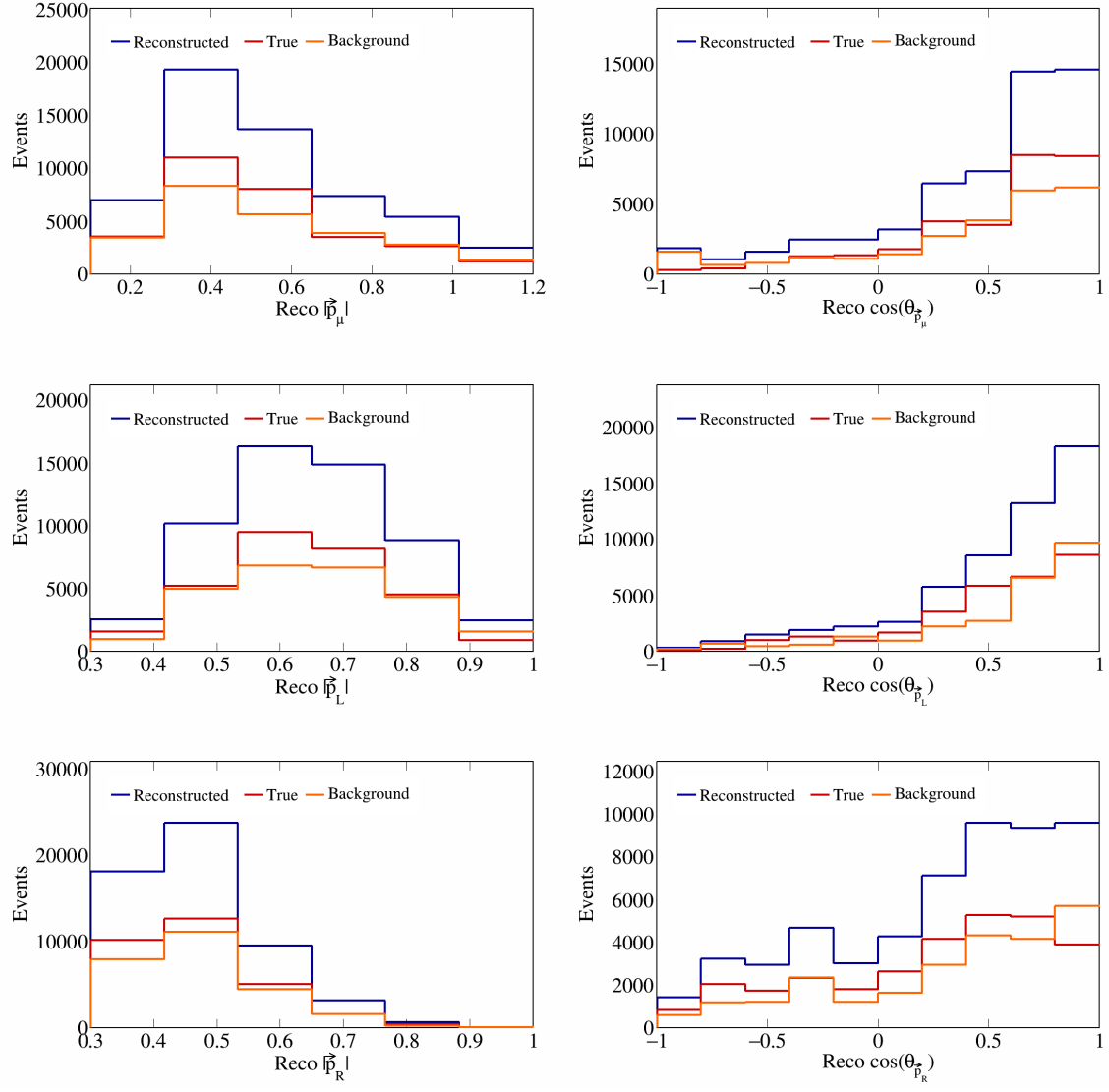


Figure 12: Vector directions and magnitudes for SBND data.

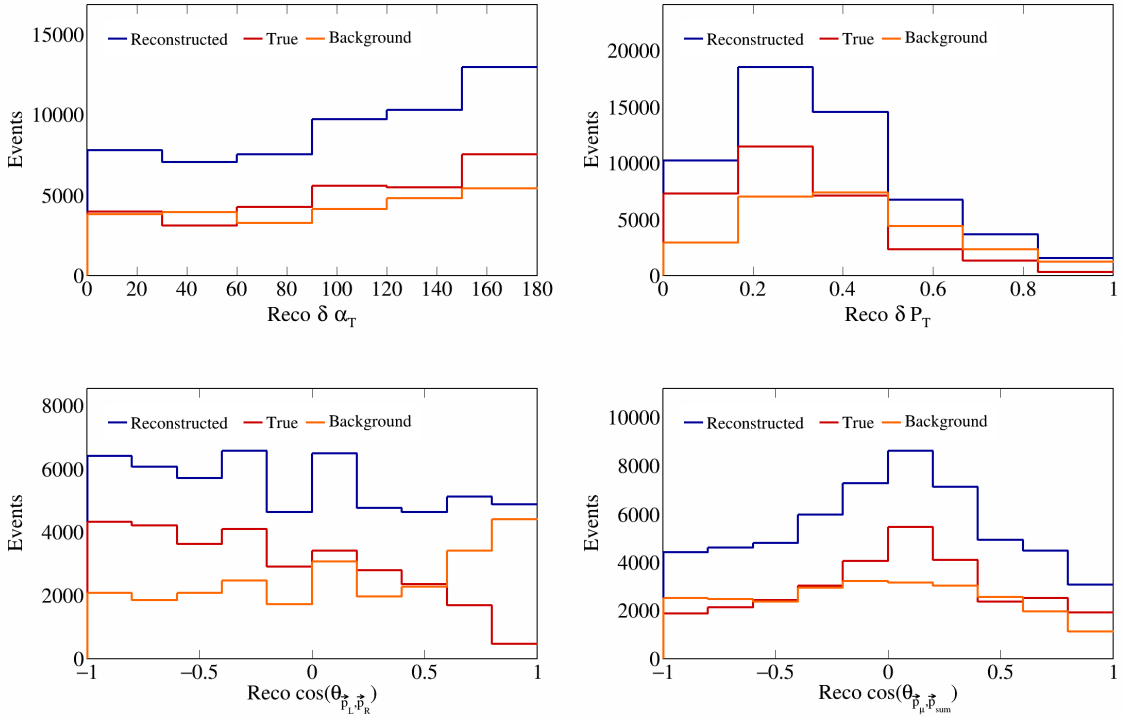


Figure 13: Vector opening angles and transverse momentum for SBND data.

160 Figure 18 and Figure 19. The migration matrices for the double differential variables (given in terms of the  
 161 bin number) are presented in Figure 20.

162 Response matrices are computed in a similar manner, but using the total number of generated events in the  
 163 denominator when computing the ratios, i.e., without requiring the events to be successfully reconstructed.  
 164 Therefore, for these matrices, the columns of the response matrices do not have to add up to 1. The response  
 165 matrices for single differential variables are presented in Figure 21 and Figure 22, and the double differential  
 166 response matrices are given in Figure 23.

### 167 3.6 Systematics

168 To include systematic uncertainties in our study, we first consider cross sectional systematics. These are  
 169 variations in the cross section models used to generate the events. They can be of two types: multisigma  
 170 and multisim. For the former, we consider a  $1\sigma$  variation of the affected parameters, and in the latter we  
 171 consider one hundred universes, each with a random variation picked from a Gaussian distribution between  
 172  $0\sigma$  and  $1\sigma$ . From these variations, we compute the covariance matrix as

$$173 E_{i,j} = \frac{1}{N_{\text{Univ}}} \sum_{s=1}^{N_{\text{Univ}}} (\tilde{\sigma}_i^{\text{Var},s} - \tilde{\sigma}_i^{\text{CV}})(\tilde{\sigma}_j^{\text{Var},s} - \tilde{\sigma}_j^{\text{CV}}) \quad (7)$$

173 where  $\tilde{\sigma}_i^{\text{Var},s}$  represents the variation cross section of the variable in the  $i$ -th bin in the  $s$ -th universe, and  
 174  $\tilde{\sigma}_i^{\text{CV}}$  is the central value (without any variation) of the cross section in the  $i$ -th bin. Then, the fractional  
 175 covariance matrix is defined as

$$176 F_{i,j} = \frac{E_{i,j}}{\tilde{\sigma}_i^{\text{CV}} \tilde{\sigma}_j^{\text{CV}}}. \quad (8)$$

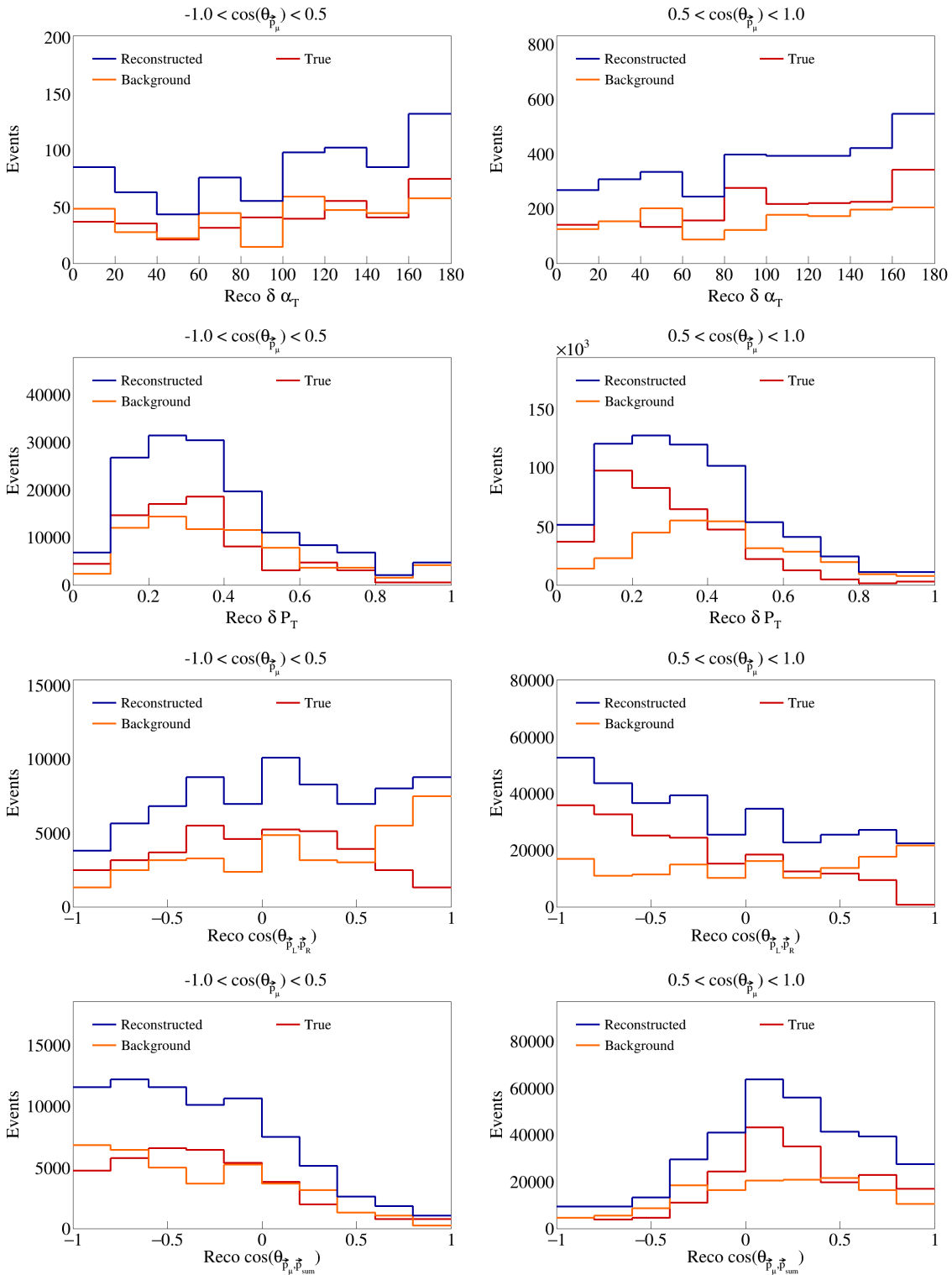


Figure 14: Sliced double differential plots for SBND events.

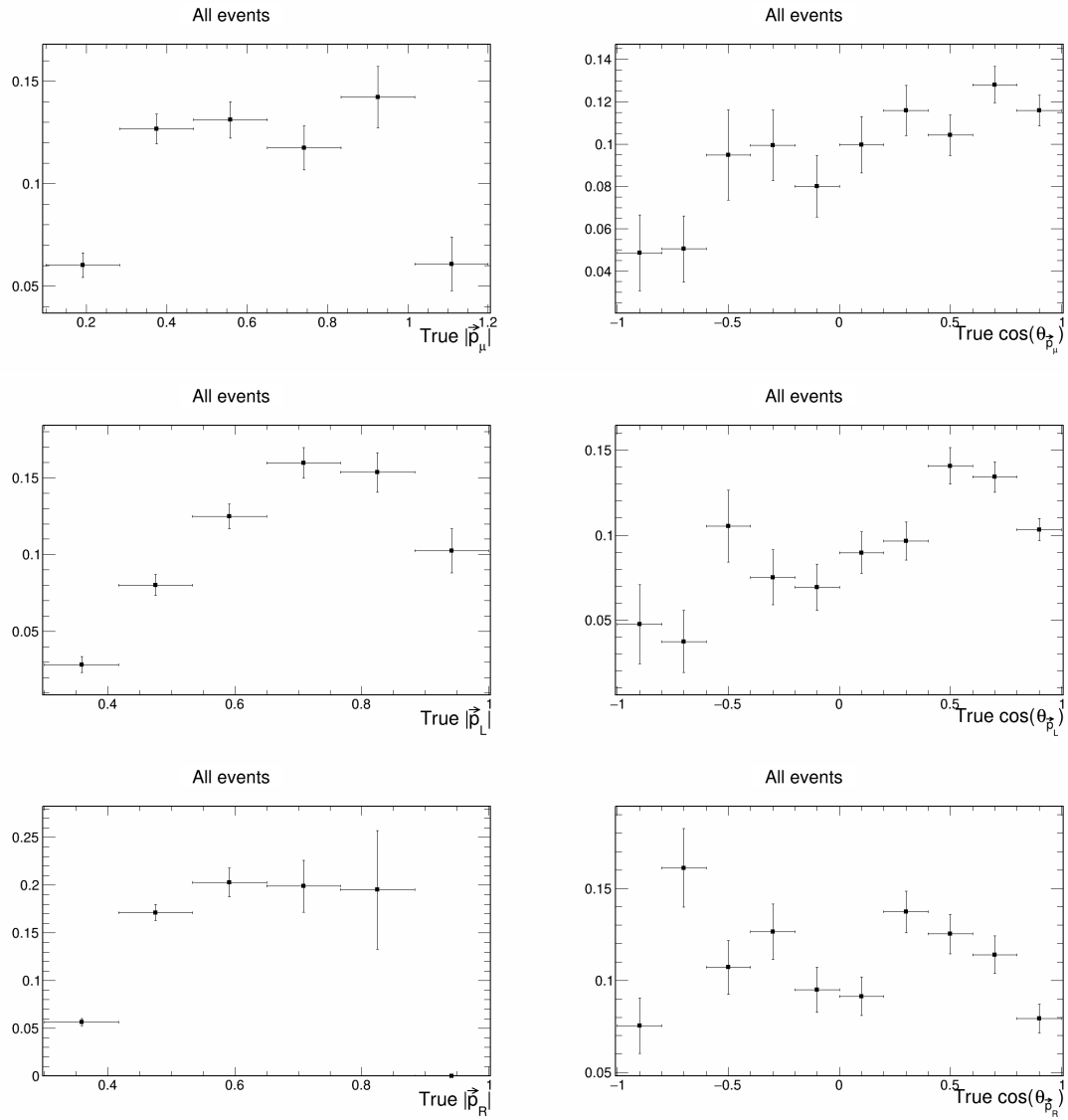


Figure 15: Signal efficiency plots for single differential vector directions and magnitudes.

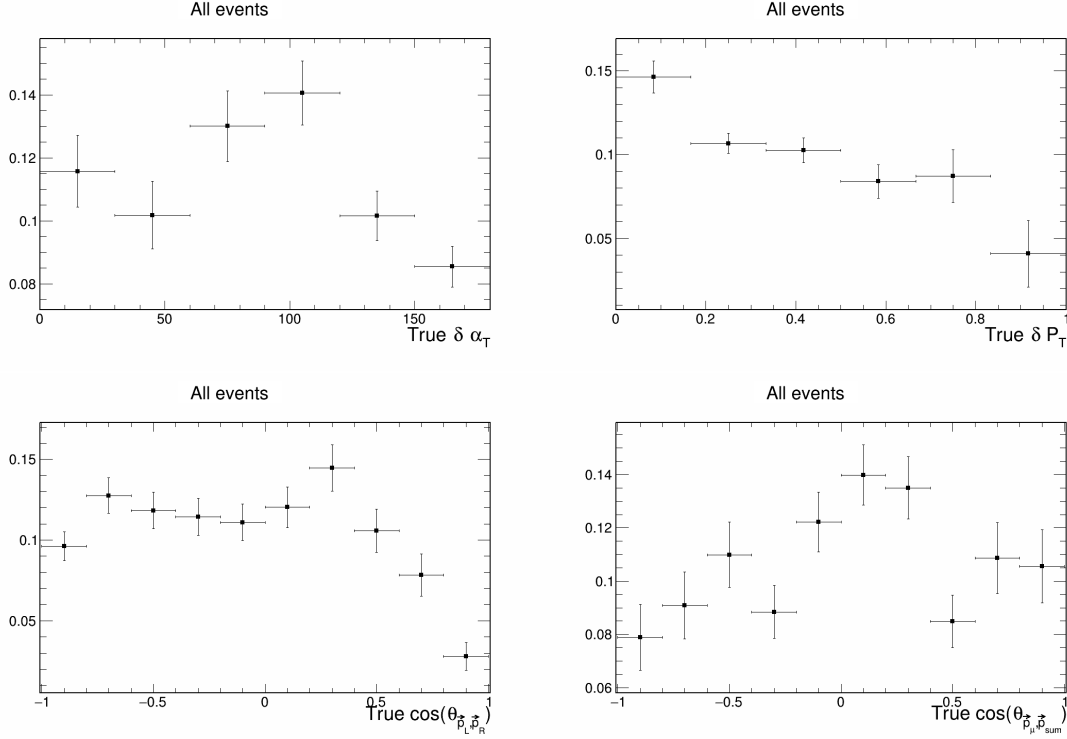


Figure 16: Signal efficiency plots for single differential vector opening angles and transverse momentum.

176 And the correlation matrix is defined as

$$\rho_{i,j} = \frac{E_{i,j}}{\sqrt{E_{i,i}E_{j,j}}}. \quad (9)$$

177 In the case of a multisigma systematic,  $N_{\text{Univ}} = 1$ , and for a multisim systematic,  $N_{\text{Univ}} = 100$ . The plots  
178 for all the individual cross sectional systematics are shown in Appendix 6.1. There are a few systematics  
179 that are currently crashing when trying to produce all plots. This are:

- 180 • MINERvAq0q3Weighting\_SBND\_v1\_Mnv2p2hGaussEnhancement
- 181 • MiscInteractionSysts\_SBND\_v1\_nuenuubar\_xsec\_ratio
- 182 • MiscInteractionSysts\_SBND\_v1\_nuenumu\_xsec\_ratio
- 183 • NOvAStyleNonResPionNorm\_SBND\_v1\_NR\_nu\_np\_CC\_1Pi

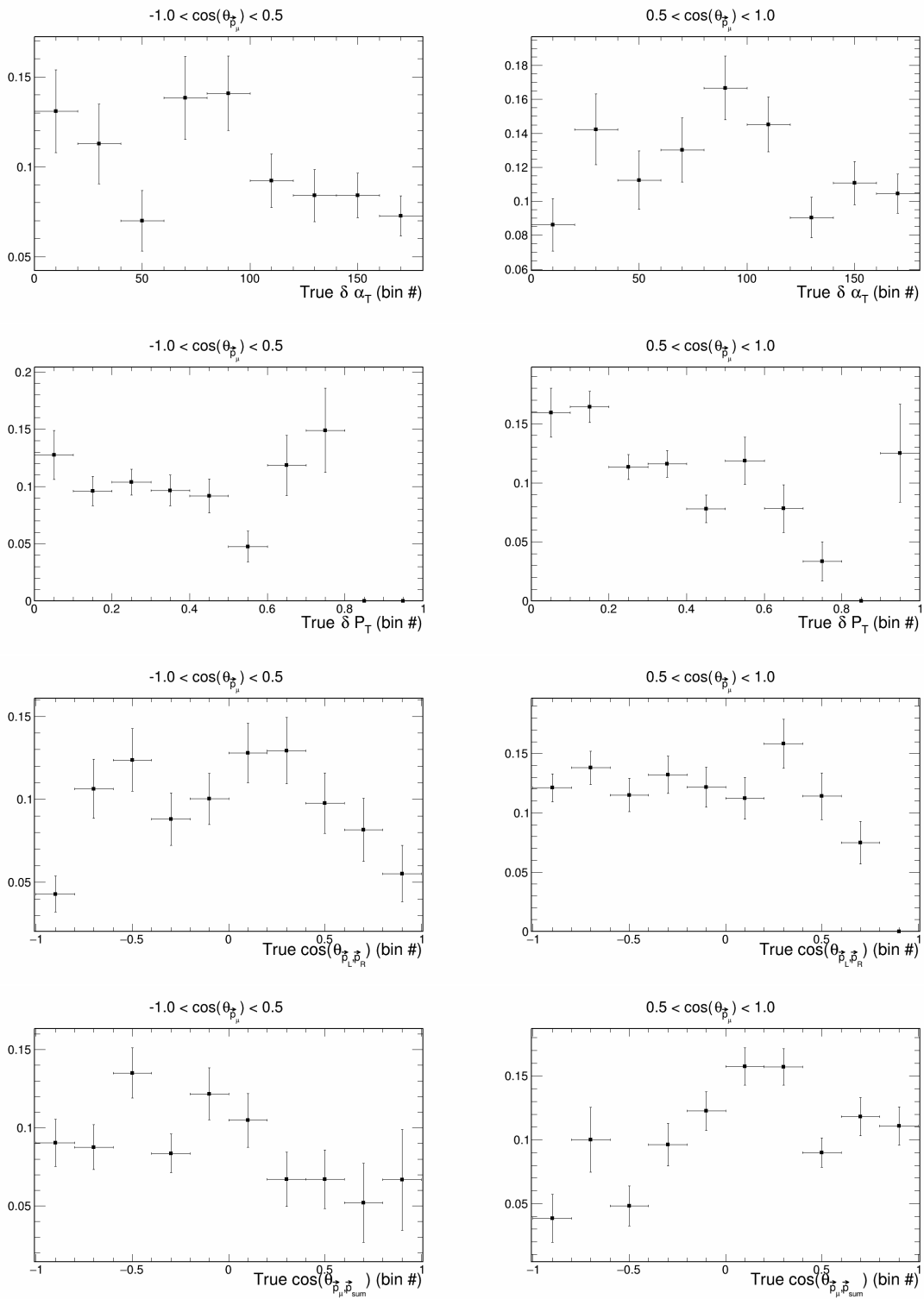


Figure 17: Signal efficiency plots for double differential variables.

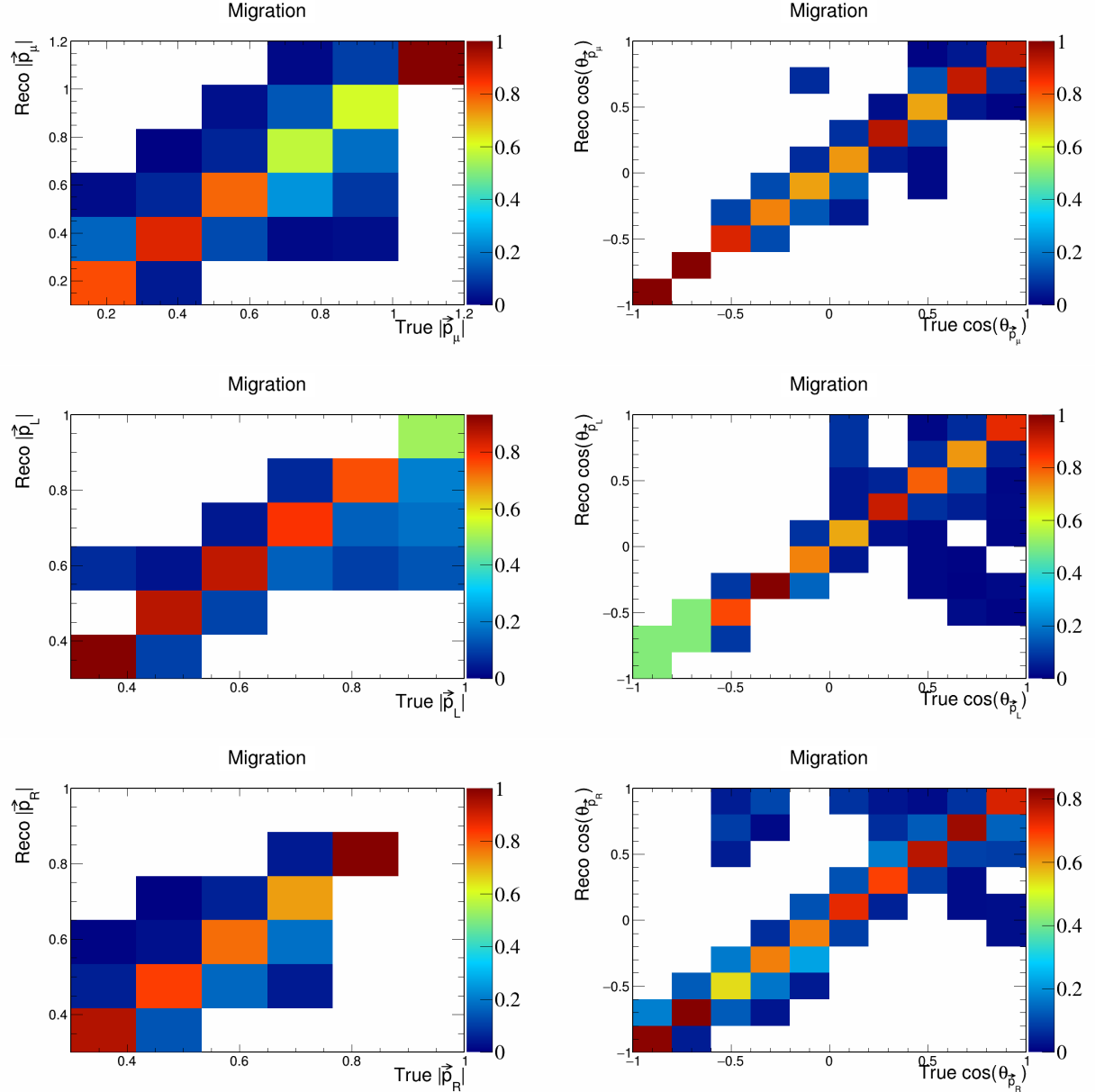


Figure 18: Migration matrices for signal differential vector directions and magnitudes.

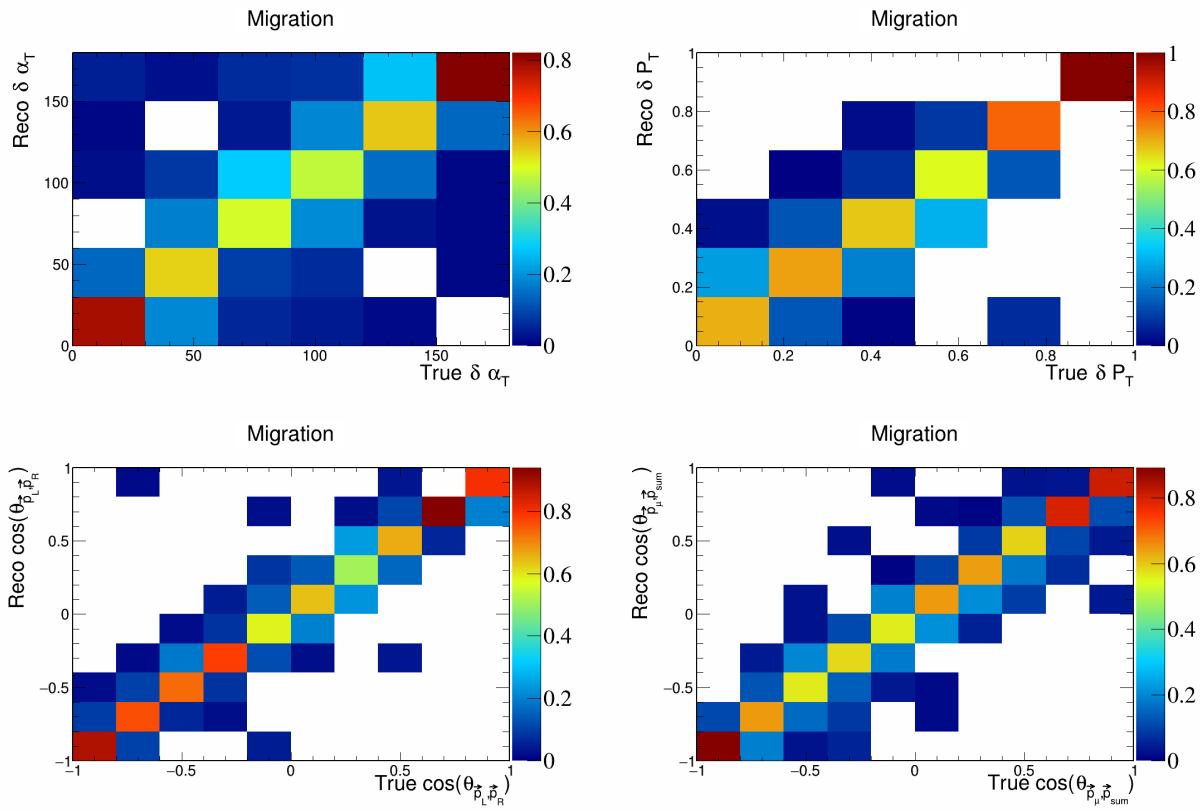


Figure 19: Migration matrices for signal differential vector opening angles and transverse momentum.

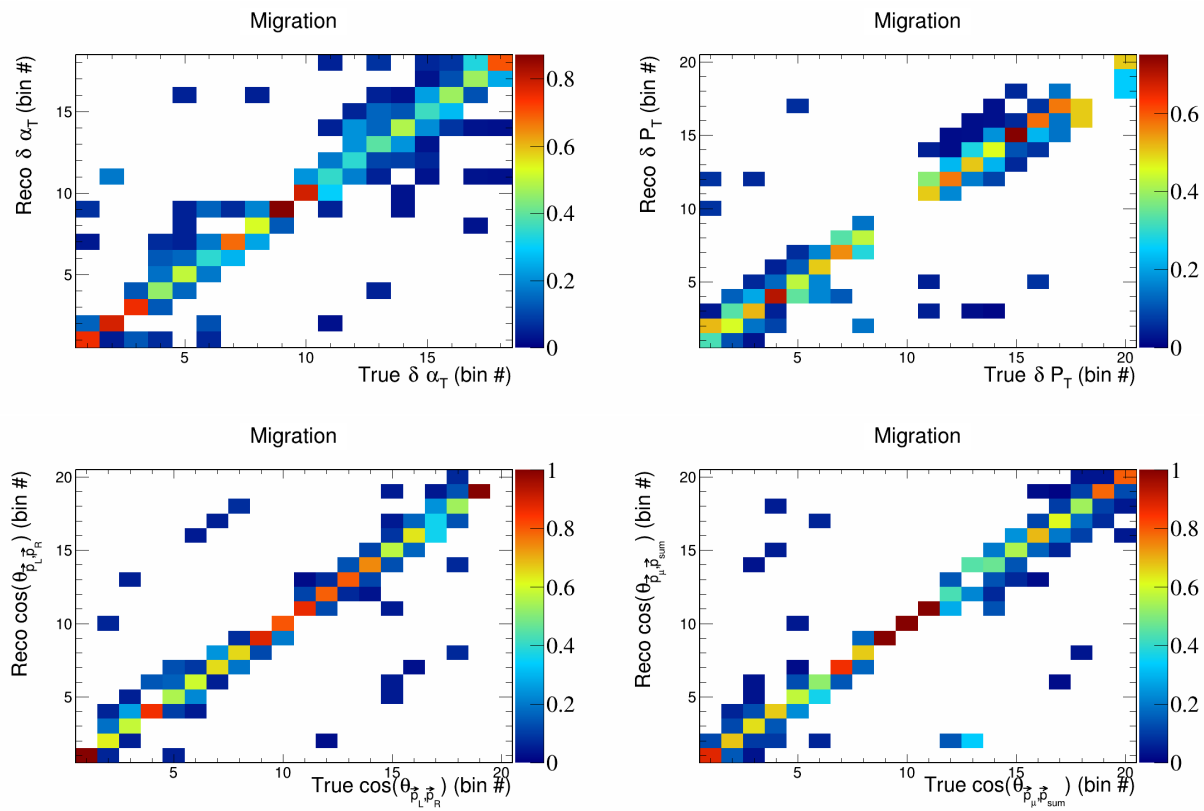


Figure 20: Migration matrices for double differential variables.

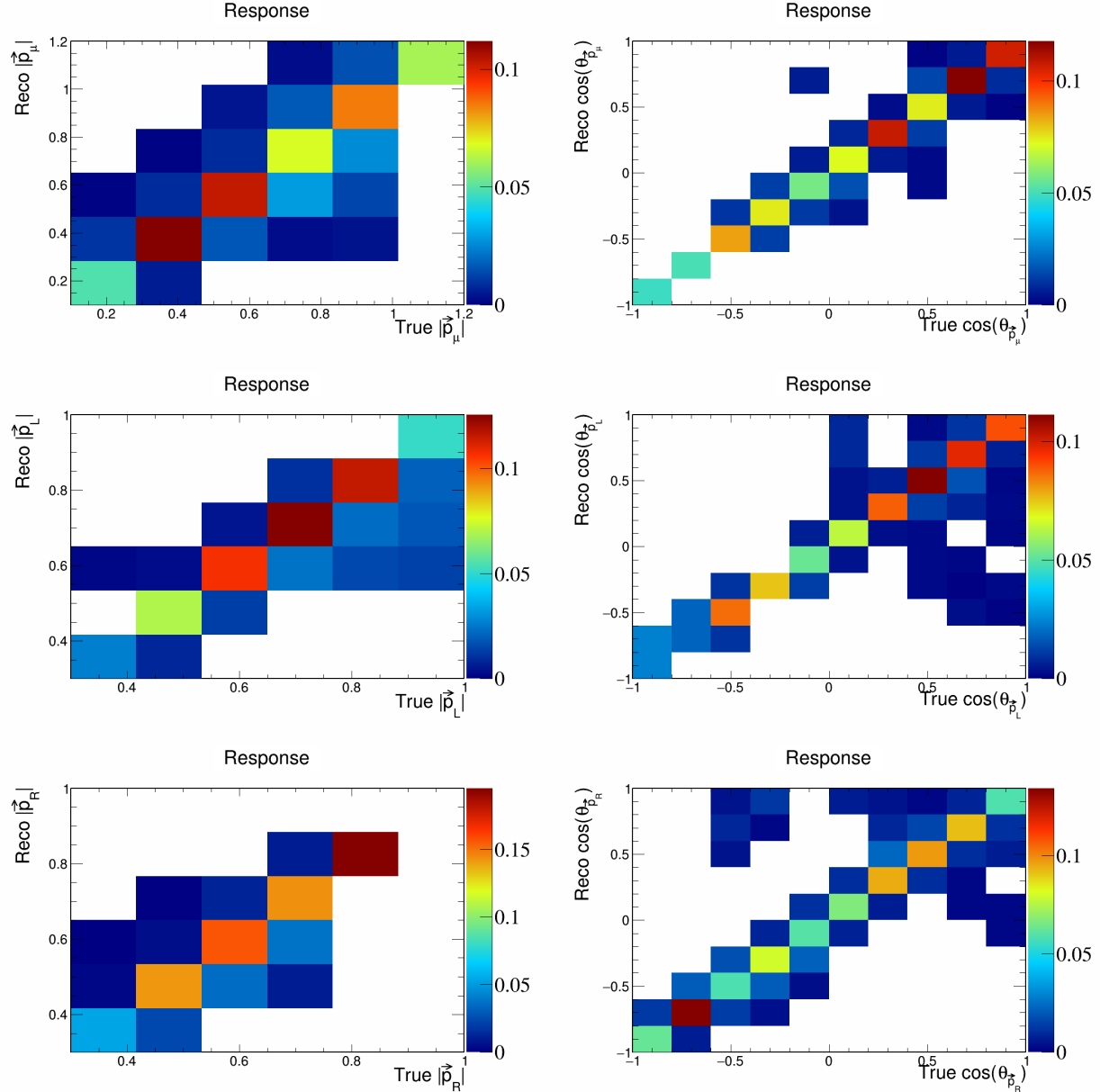


Figure 21: Response matrices for signal differential vector directions and magnitudes.

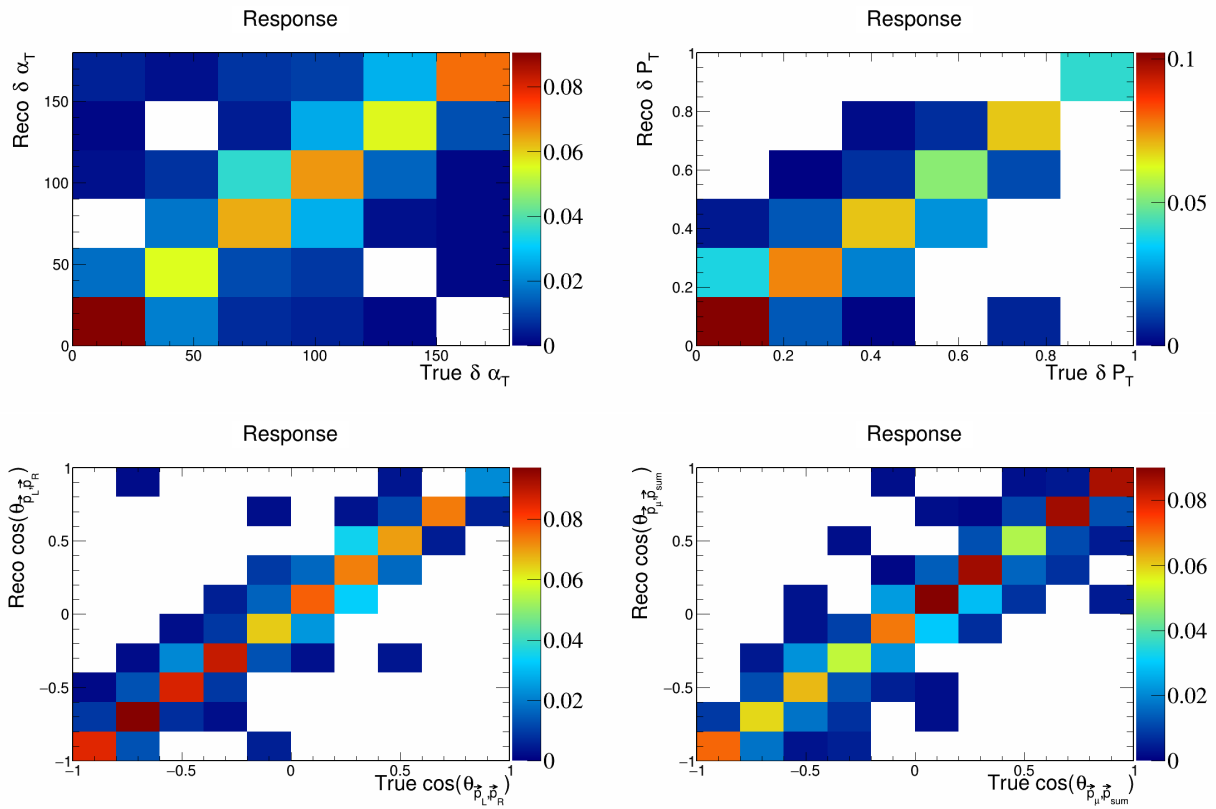


Figure 22: Response matrices for signal differential vector opening angles and transverse momentum.

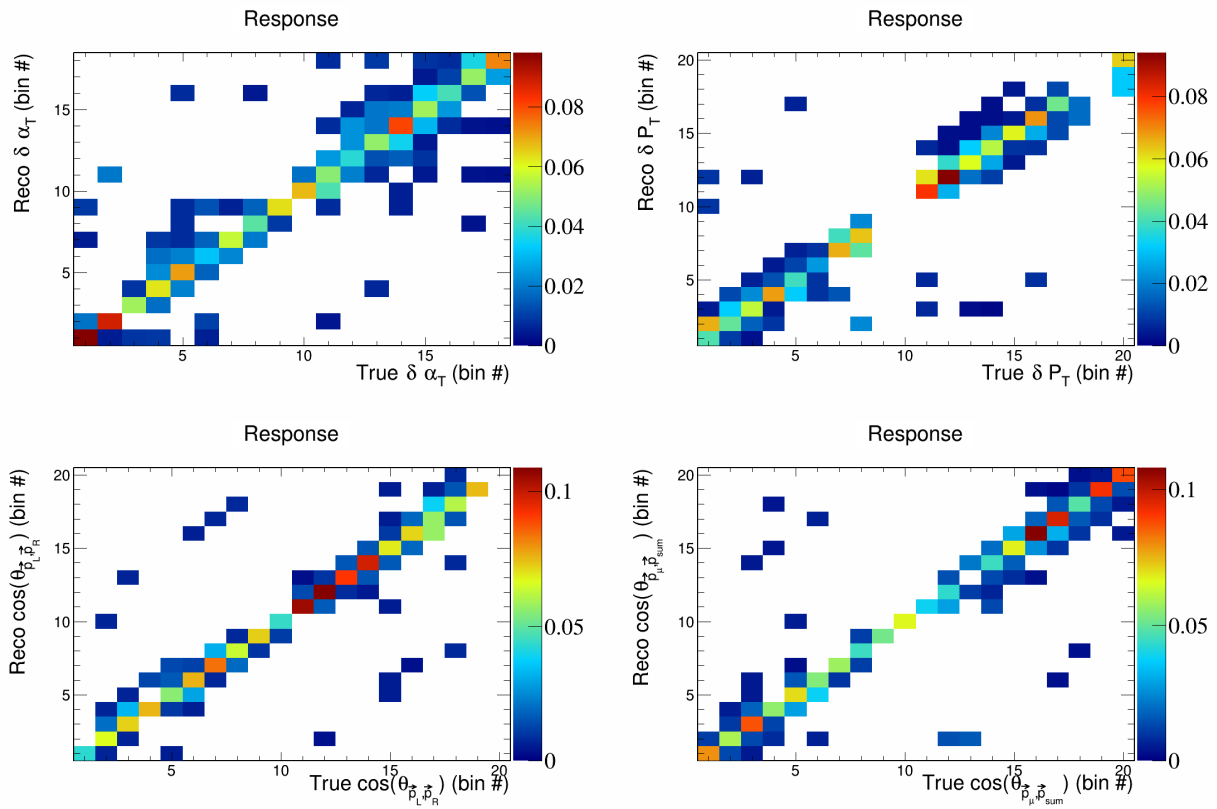


Figure 23: Response matrices for double differential variables.

<sub>184</sub> **4 Closure test**

<sub>185</sub> To ensure that the unfolding techniques that we will implement work correctly, we perform a closure test,  
<sub>186</sub> meaning that we will perform the unfolding on simulated true signal events and check that the unfolded  
<sub>187</sub> data matches the true signal data with added smearing. We can see that the plots that perform this test  
<sub>188</sub> in Figure 24 and Figure 25. We also note that the overall shape and magnitude of our histograms match  
<sub>189</sub> previously reported MicroBooNE analyses. **TODO: stop using dummy covariance matrices.**

<sub>190</sub> **5 Cross-section results**

<sub>191</sub> Placeholder.

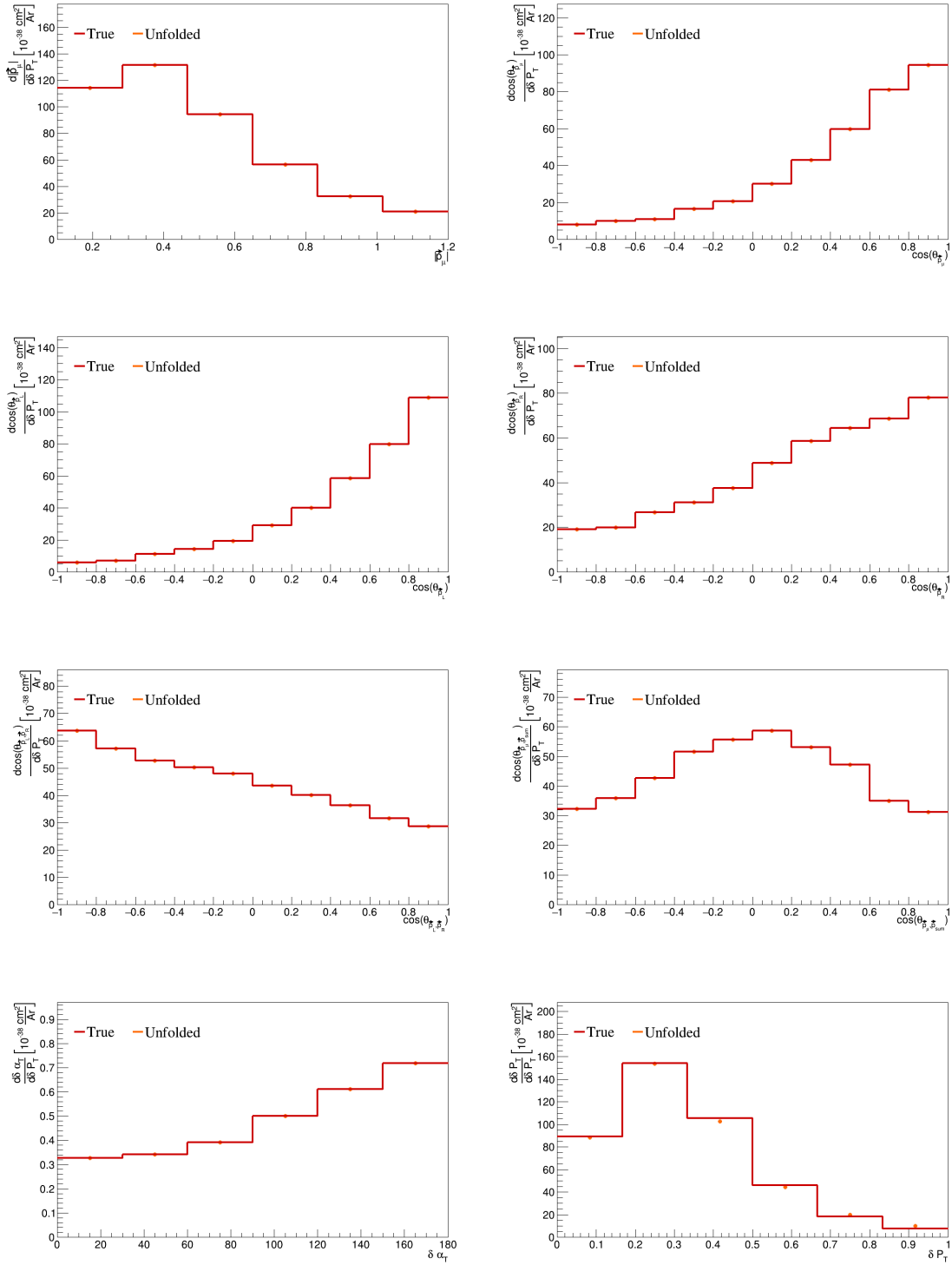


Figure 24: Closure test single differential plots.

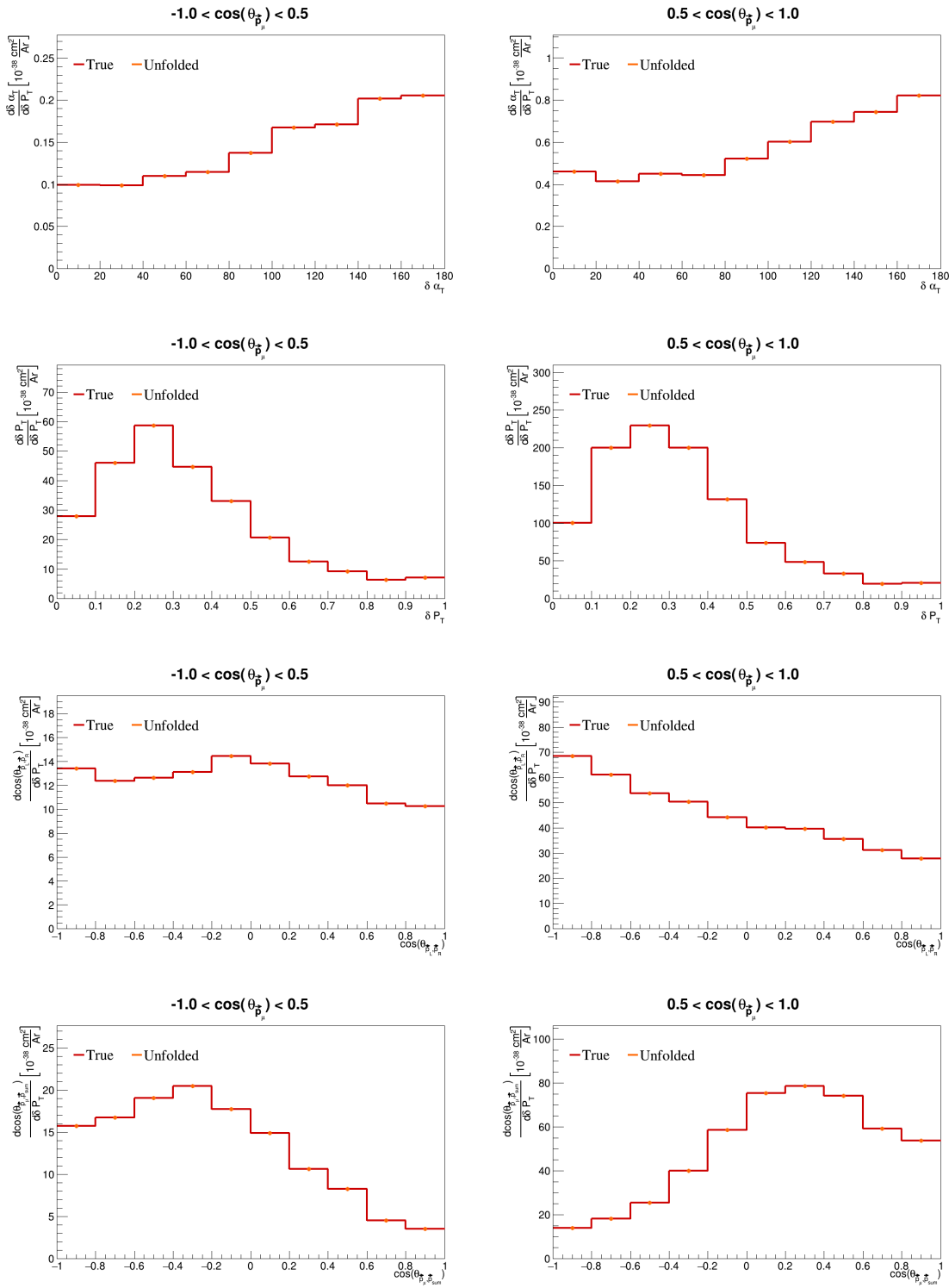


Figure 25: Closure test double differential plots.

## 192 6 Appendices

### 193 6.1 Cross section systematics

194 In this appendix, the variations, covariance matrices, fractional covariance matrices, and correlation matrices  
 195 are plotted for all of the cross section systematics and variables.

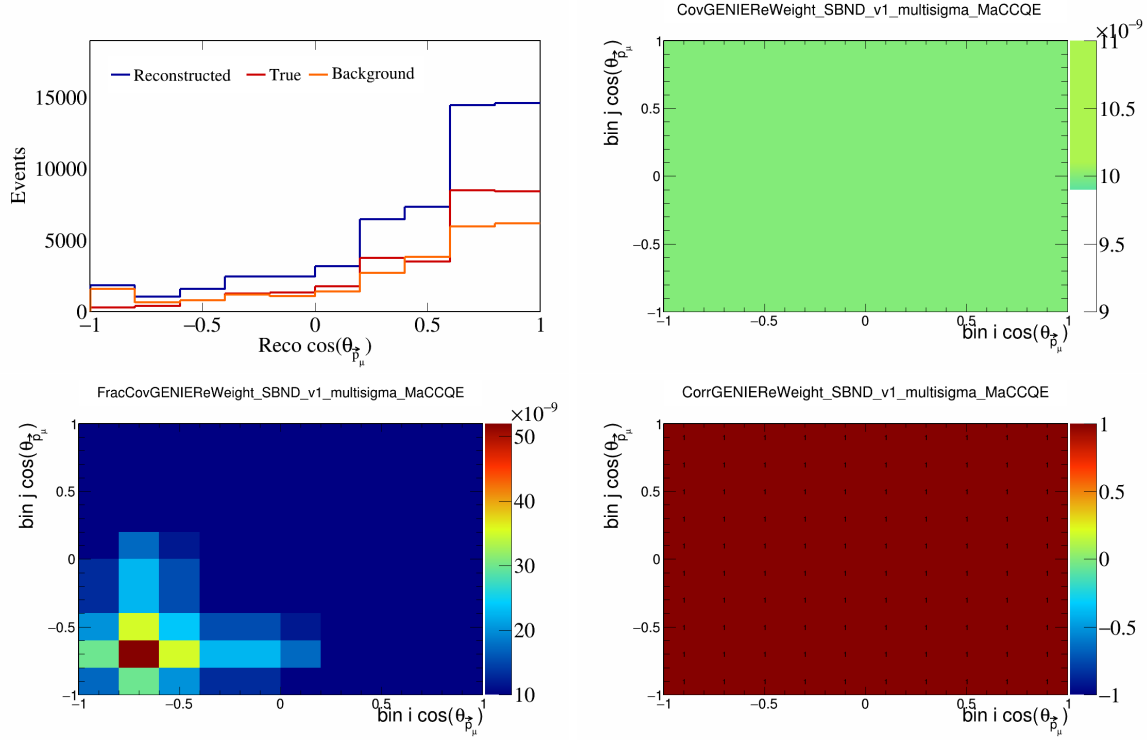


Figure 26: GenieMaCCQE variations for  $\cos(\theta_{\vec{p}_\mu})$ .

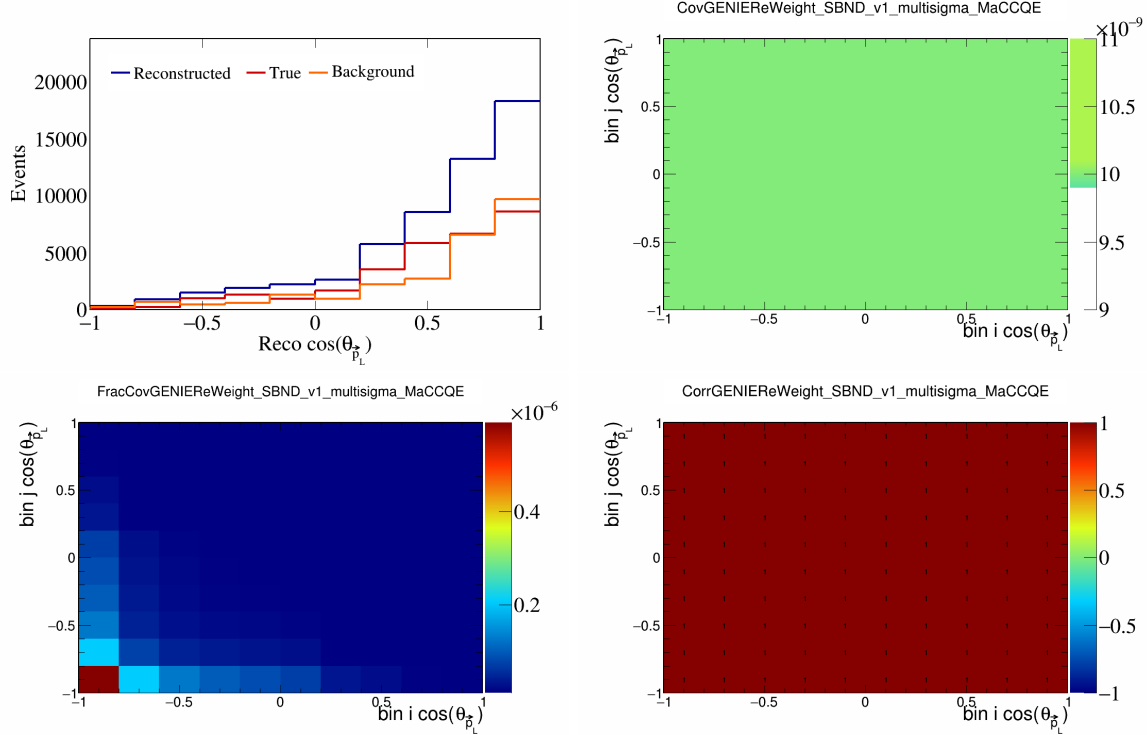


Figure 27: GenieMaCCQE variations for  $\cos(\theta_{\vec{p}_L})$ .

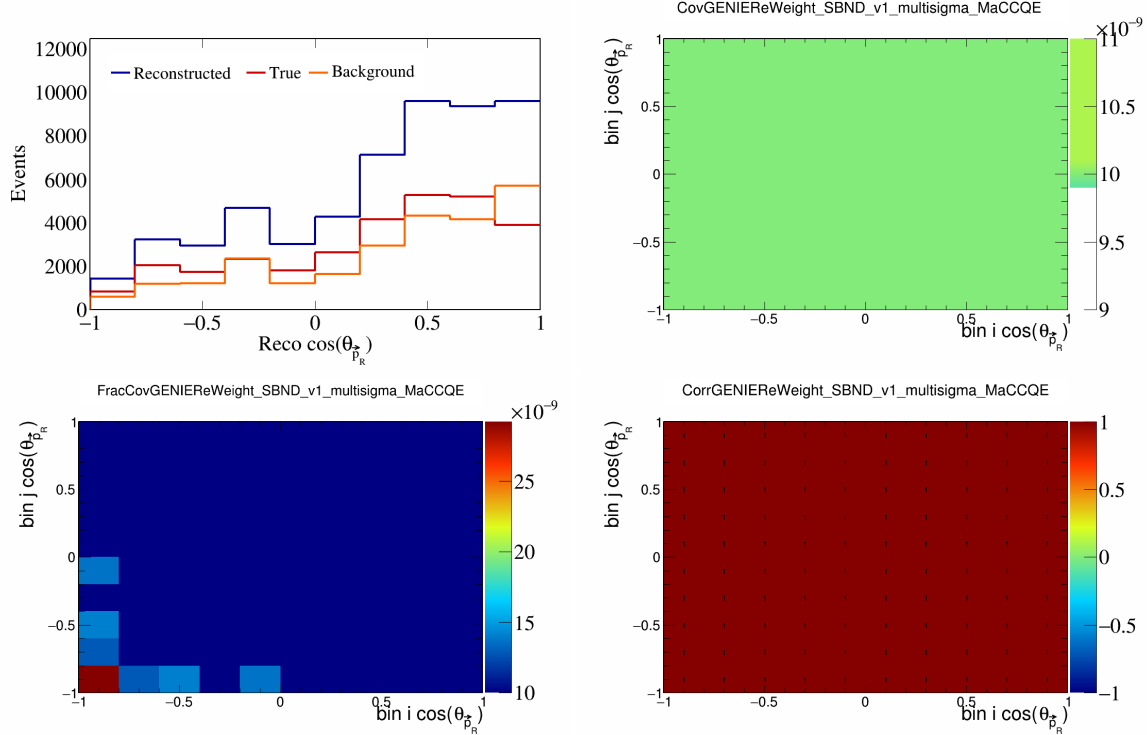


Figure 28: GenieMaCCQE variations for  $\cos(\theta_{\vec{p}_R})$ .

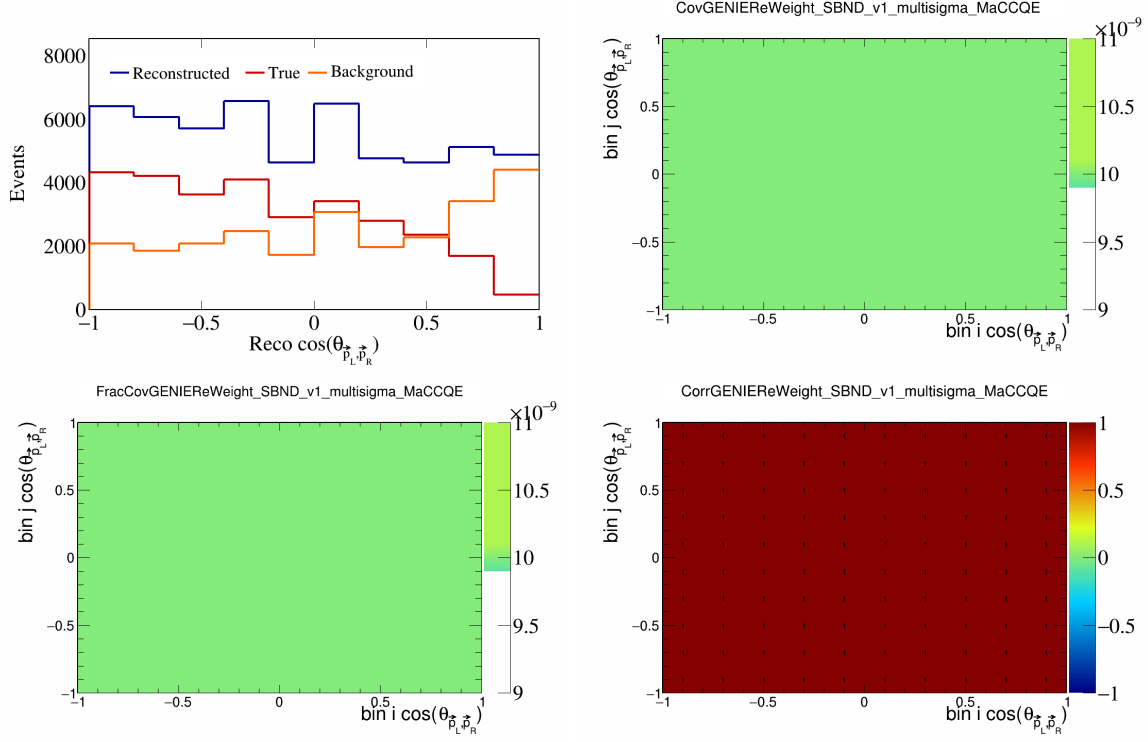


Figure 29: GenieMaCCQE variations for  $\cos(\theta_{\vec{p}_L, \vec{p}_R})$ .

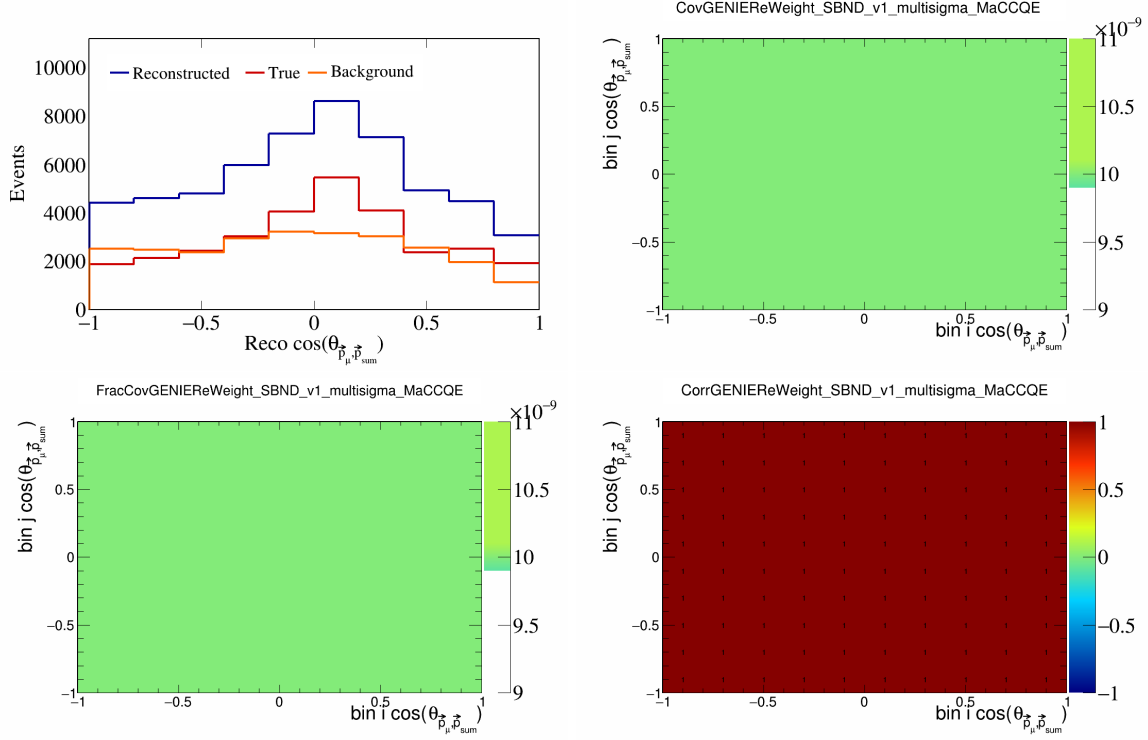


Figure 30: GenieMaCCQE variations for  $\cos(\theta_{\vec{p}_\mu, \vec{p}_{\text{sum}}})$ .

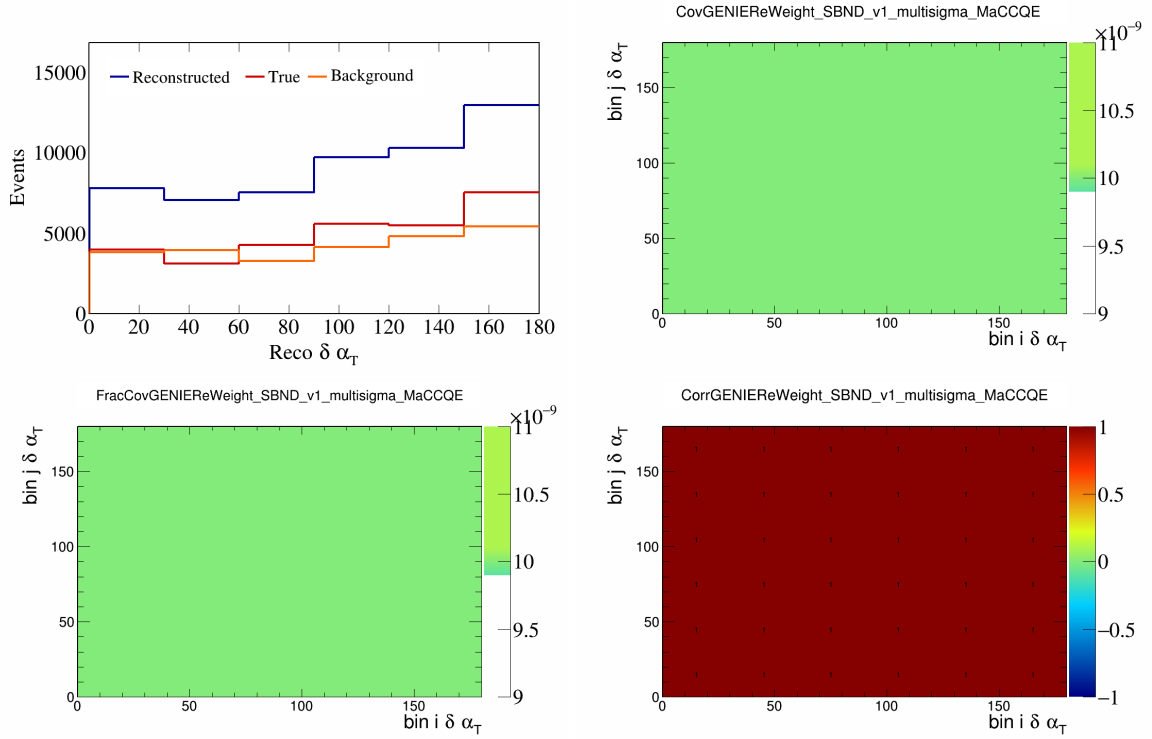


Figure 31: GenieMaCCQE variations for  $\delta\alpha_T$ .

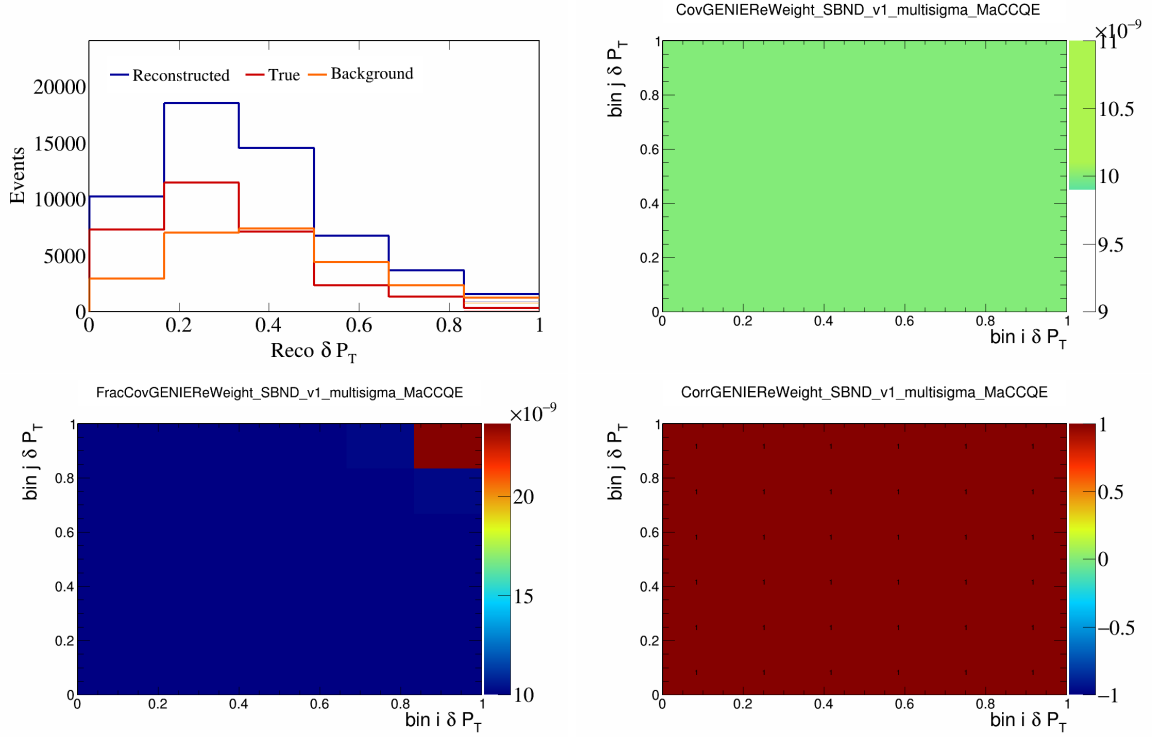


Figure 32: GenieMaCCQE variations for  $\delta P_T$ .

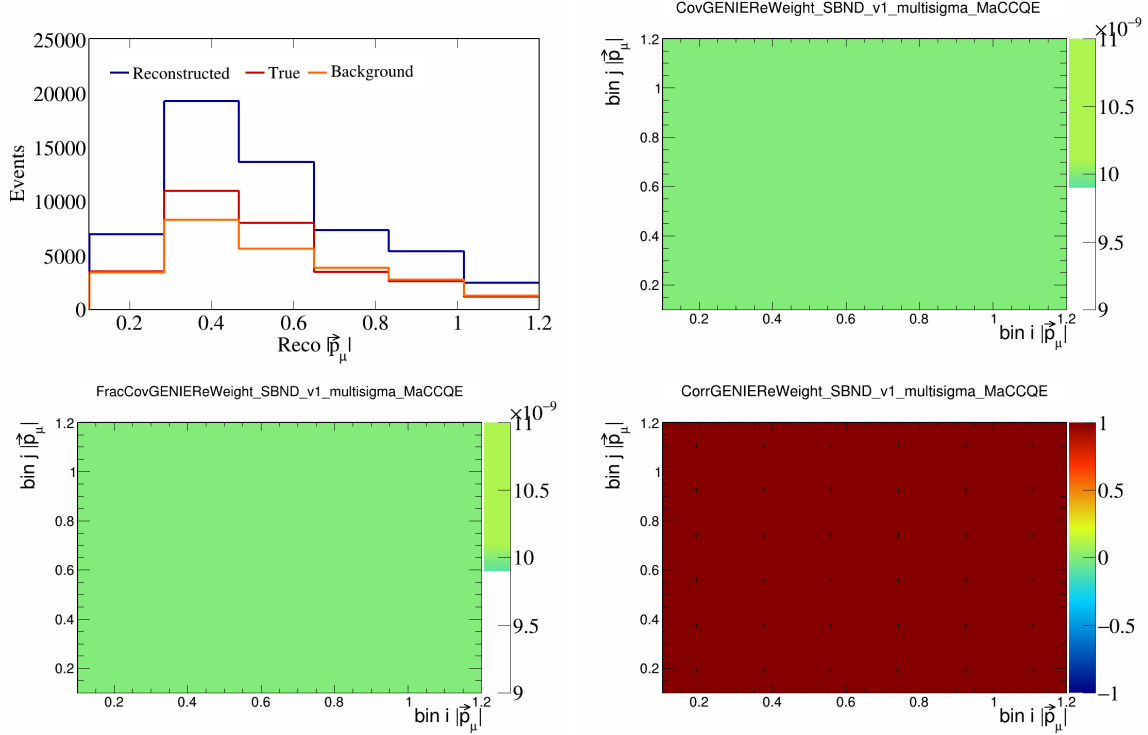


Figure 33: GenieMaCCQE variations for  $|\vec{p}_\mu|$ .

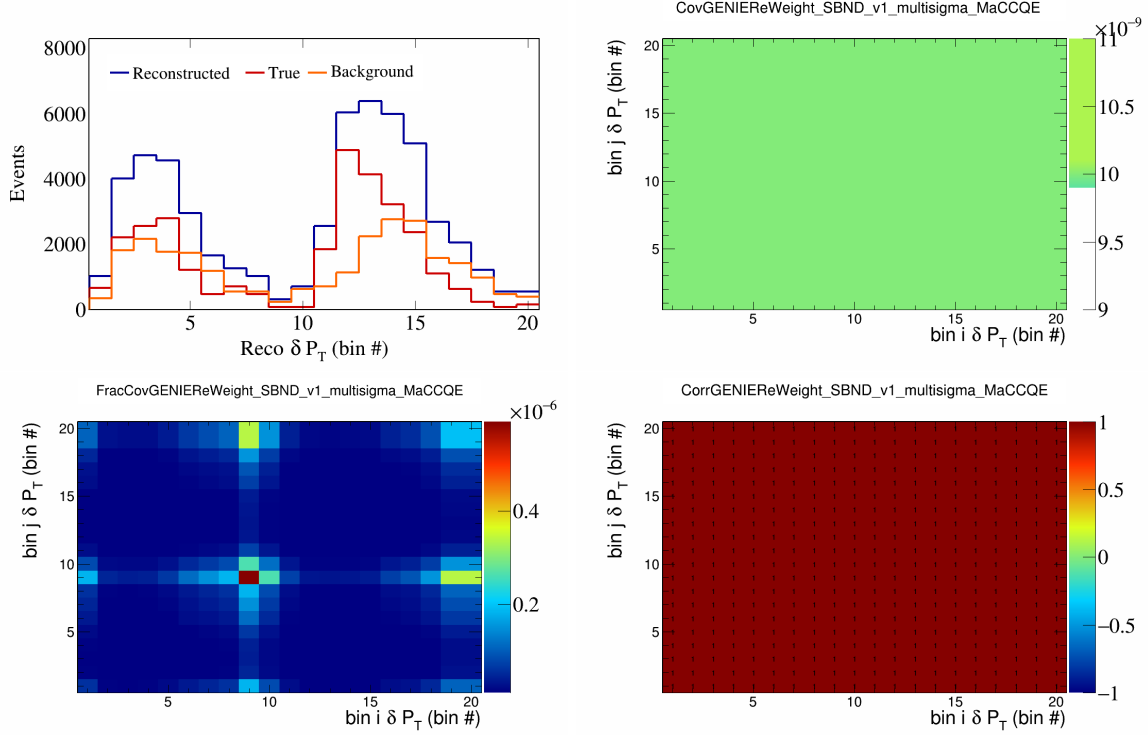


Figure 34: GenieMaCCQE variations for  $\delta P_T$  in  $\cos(\theta_{\vec{p}_\mu})$ .

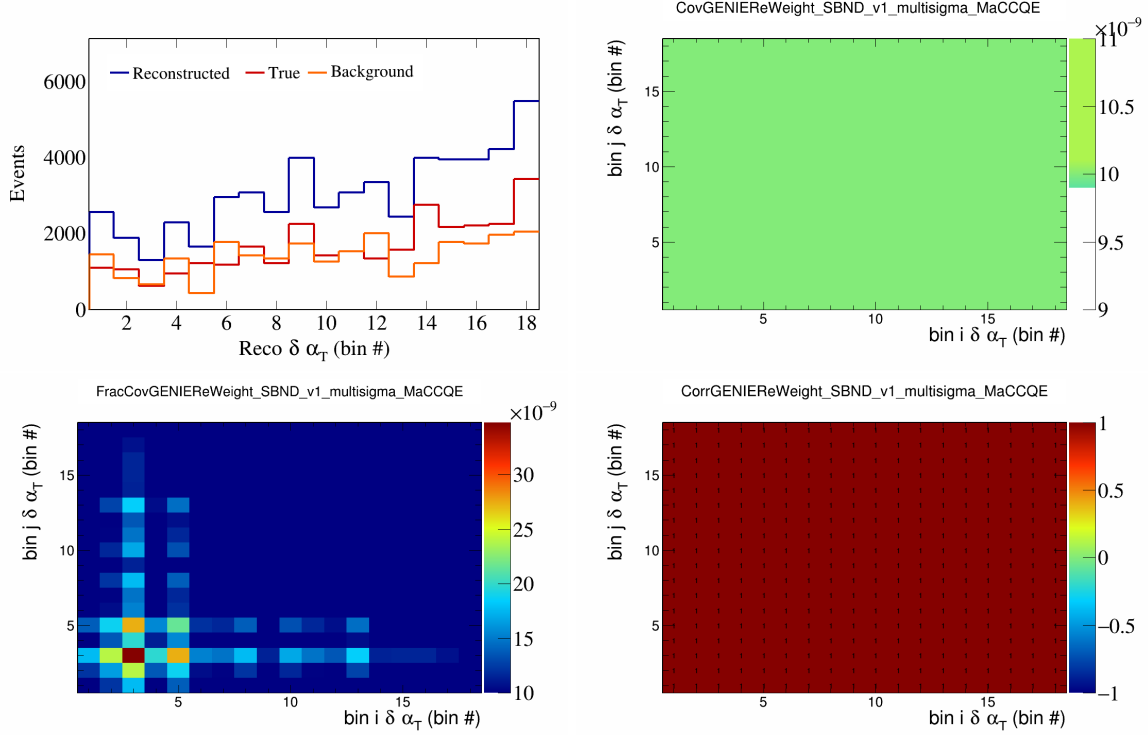


Figure 35: GenieMaCCQE variations for  $\delta\alpha_T$  in  $\cos(\theta_{\vec{p}_\mu})$ .

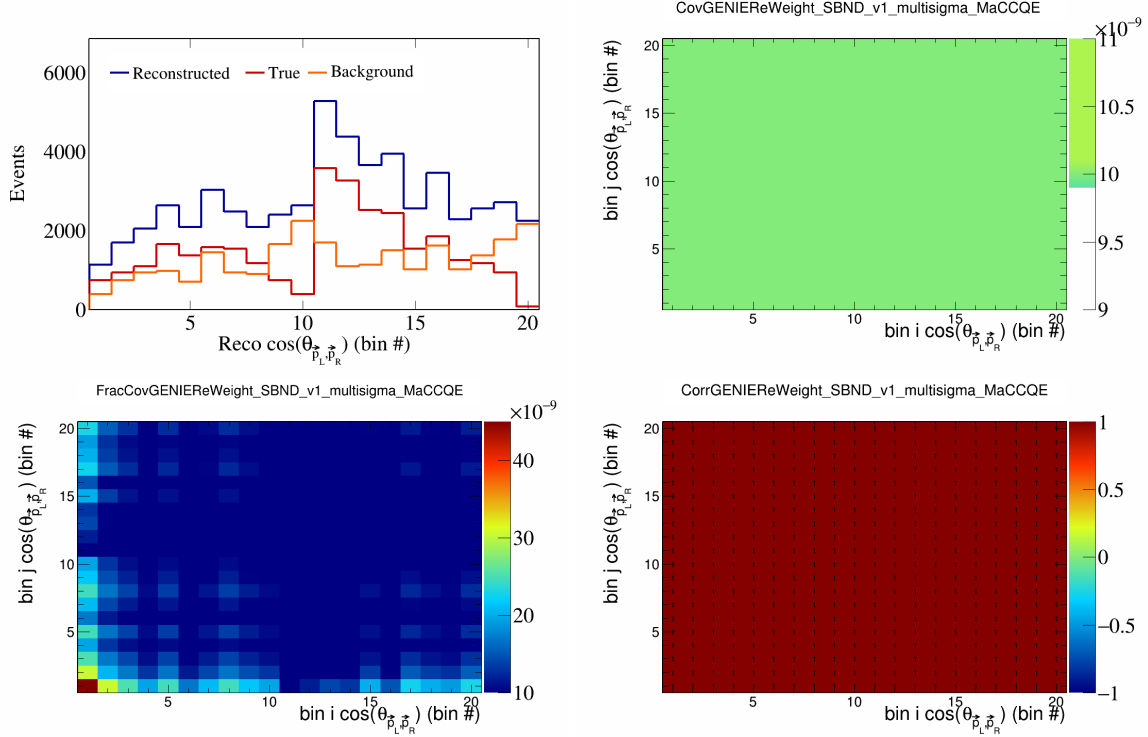


Figure 36: GenieMaCCQE variations for  $\cos(\theta_{\vec{p}_L, \vec{p}_R})$  in  $\cos(\theta_{\vec{p}_\mu})$ .

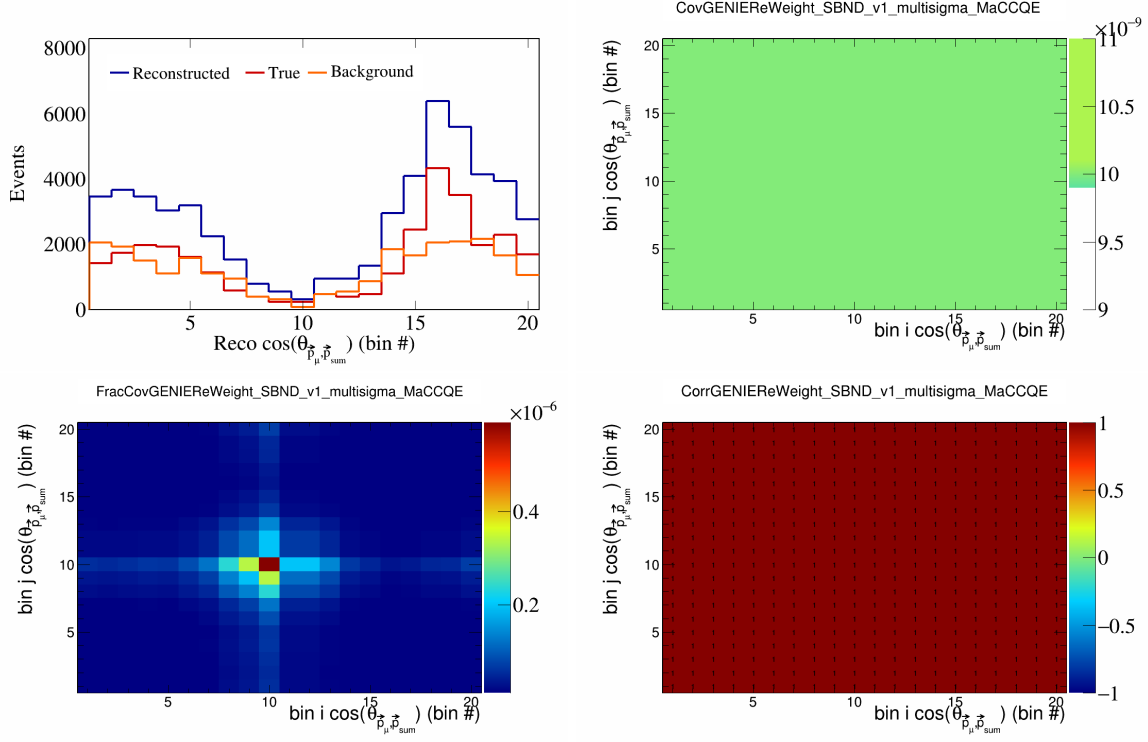


Figure 37: GenieMaCCQE variations for  $\cos(\theta_{\vec{p}_\mu, \vec{p}_{\text{sum}}})$  in  $\cos(\theta_{\vec{p}_\mu})$ .

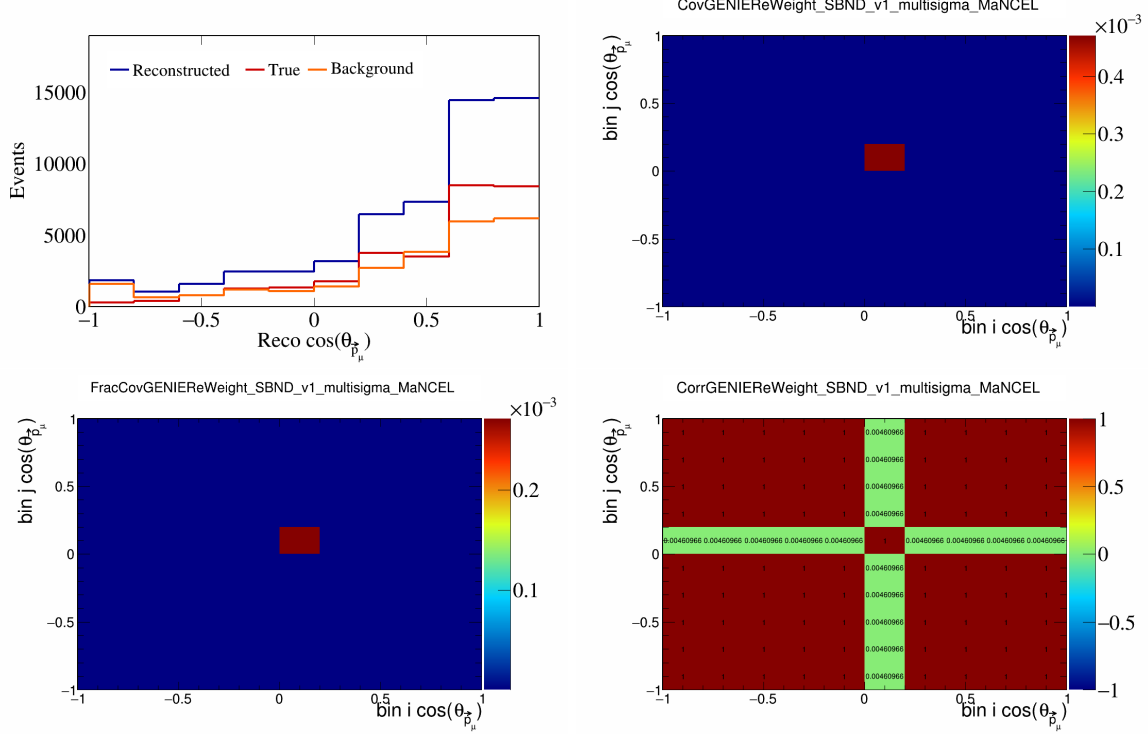


Figure 38: GenieMaNCEL variations for  $\cos(\theta_{\vec{p}_\mu})$ .

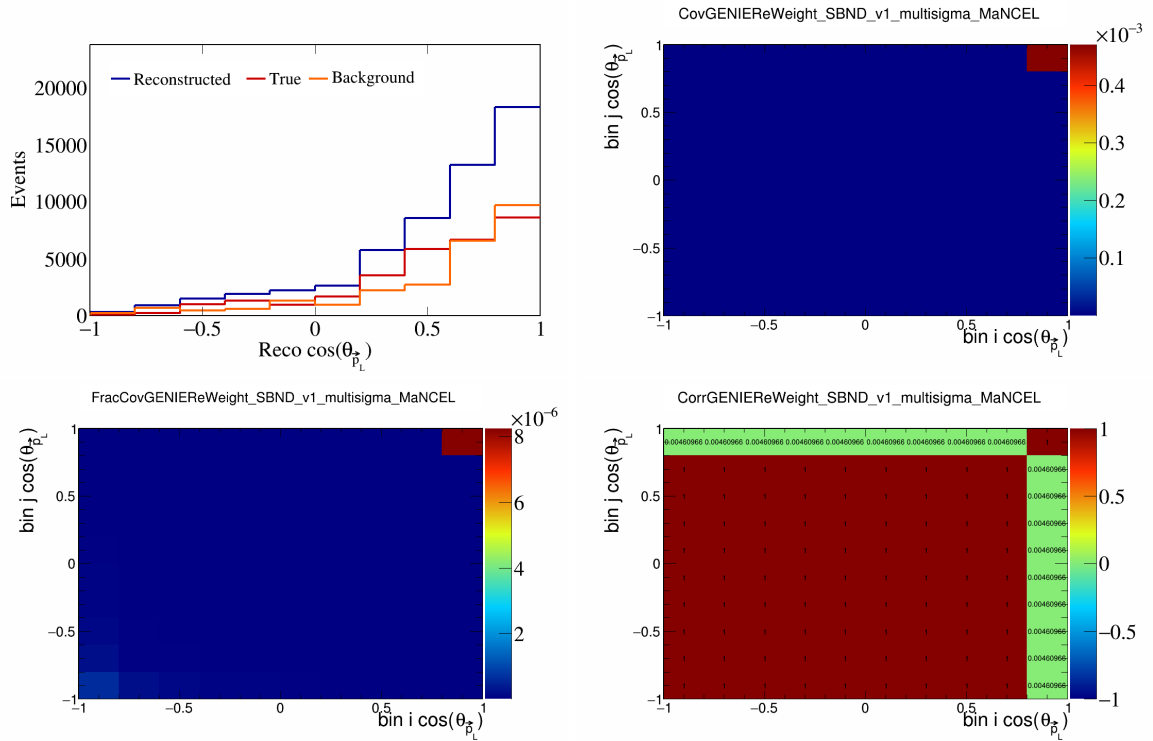


Figure 39: GenieMaNCEL variations for  $\cos(\theta_{\vec{p}_L})$ .

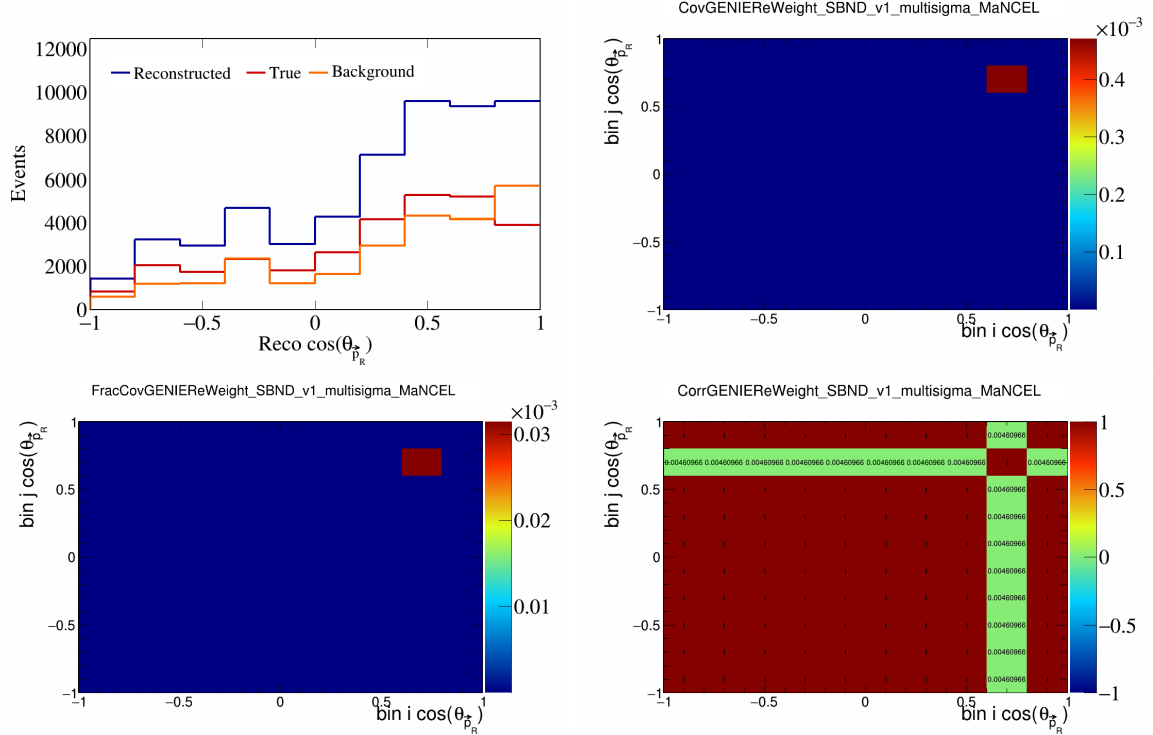


Figure 40: GenieMaNCEL variations for  $\cos(\theta_{\vec{p}_R})$ .

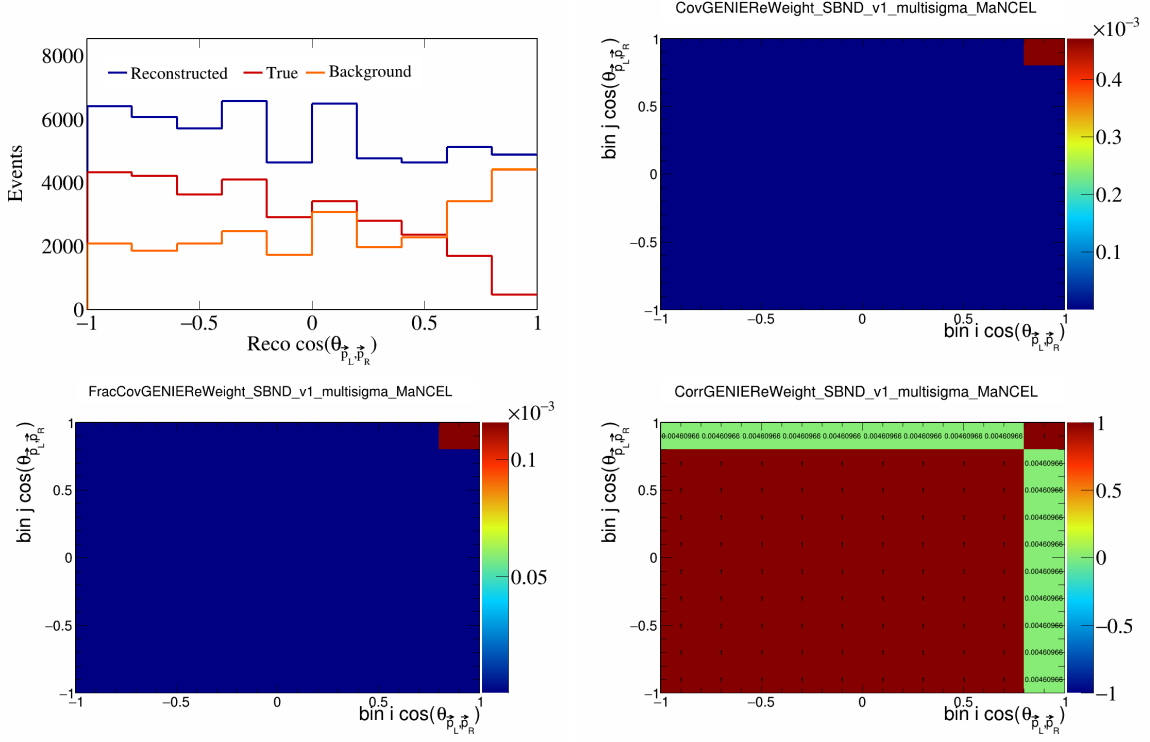


Figure 41: GenieMaNCEL variations for  $\cos(\theta_{\vec{p}_L, \vec{p}_R})$ .

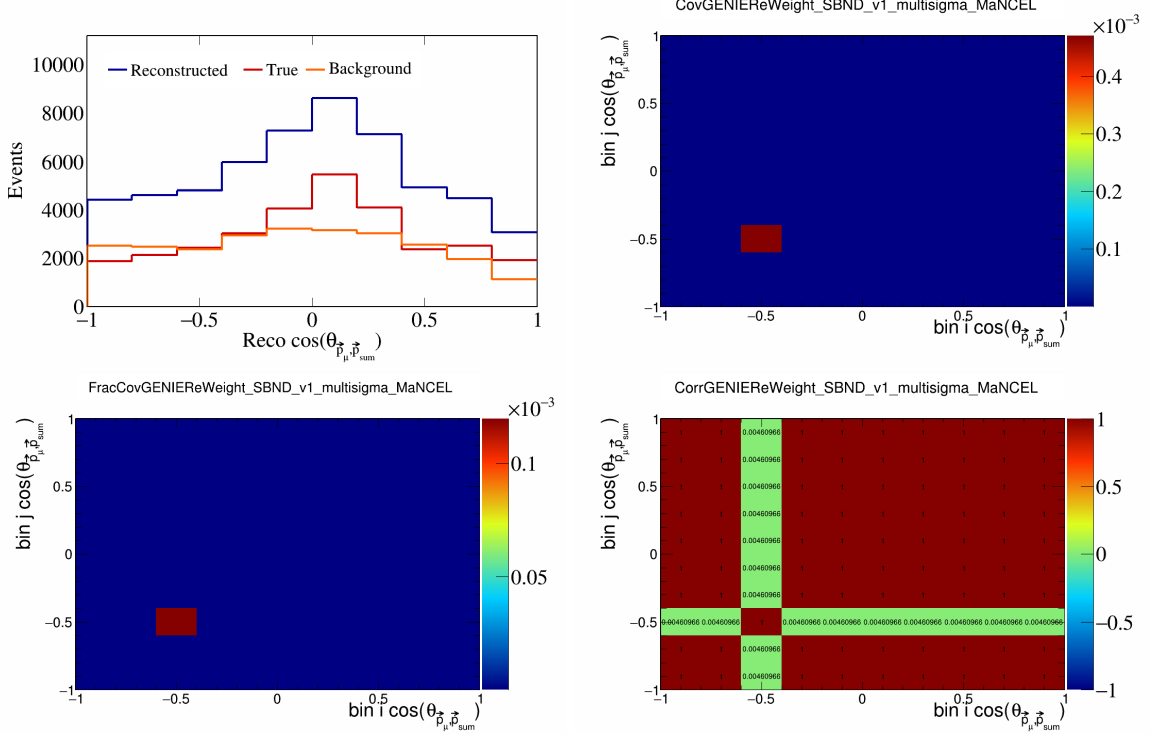


Figure 42: GenieMaNCEL variations for  $\cos(\theta_{\vec{p}_\mu, \vec{p}_{\text{sum}}})$ .

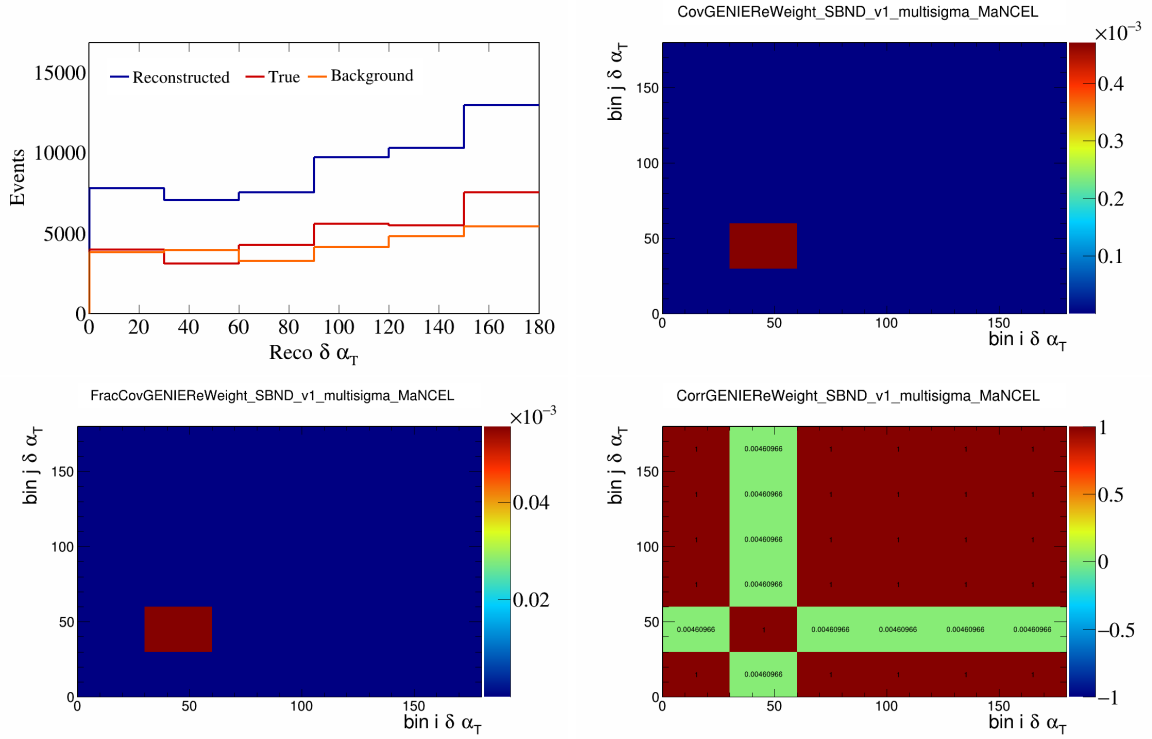


Figure 43: GenieMaNCEL variations for  $\delta\alpha_T$ .

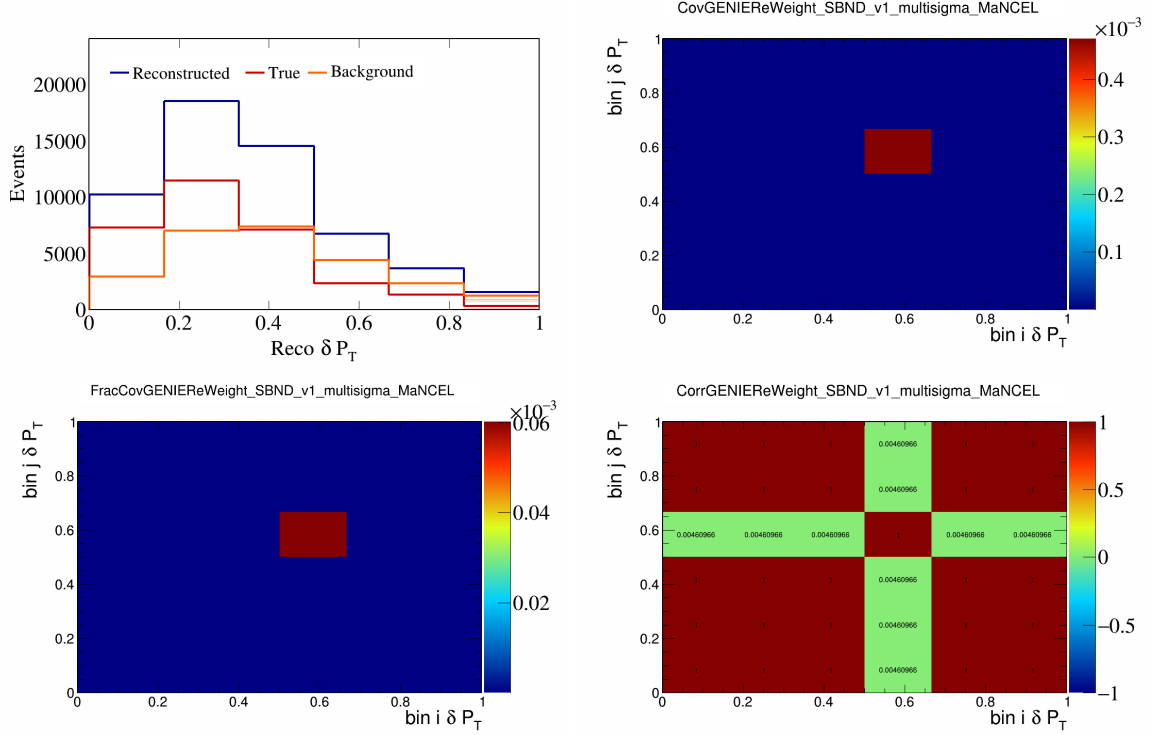


Figure 44: GenieMaNCEL variations for  $\delta P_T$ .

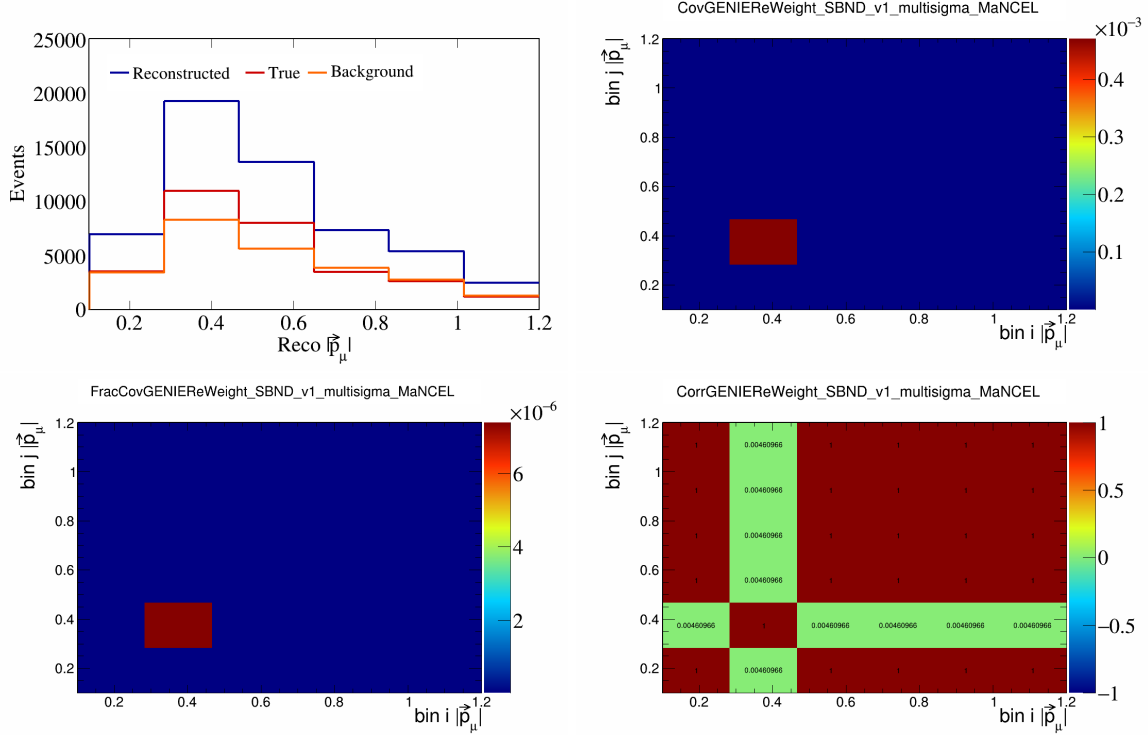


Figure 45: GenieMaNCEL variations for  $|\vec{p}_\mu|$ .

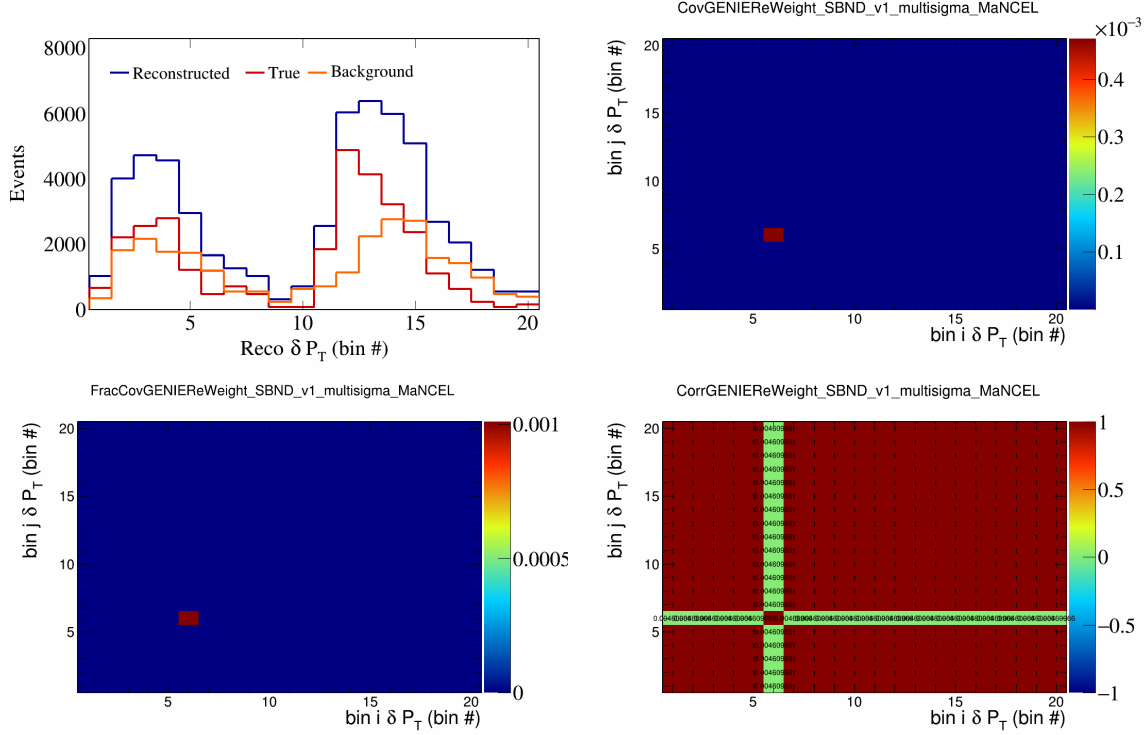


Figure 46: GenieMaNCEL variations for  $\delta P_T$  in  $\cos(\theta_{\vec{p}_\mu})$ .

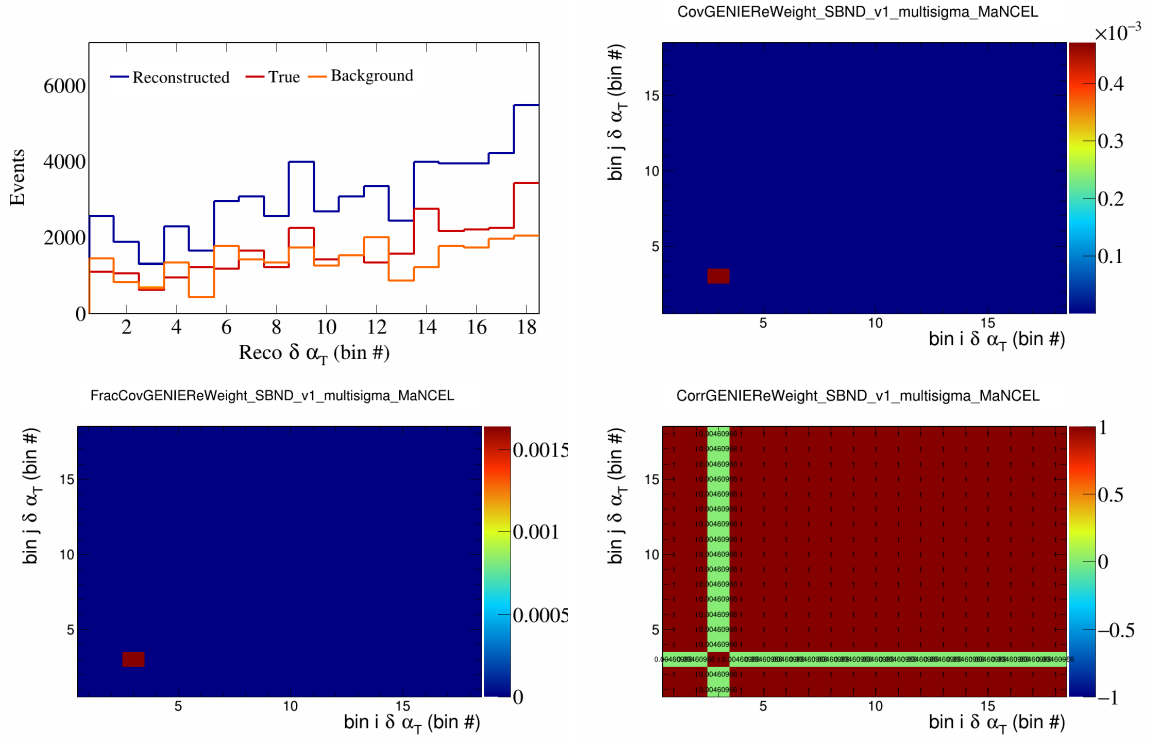


Figure 47: GenieMaNCEL variations for  $\delta\alpha_T$  in  $\cos(\theta_{\vec{p}_\mu})$ .

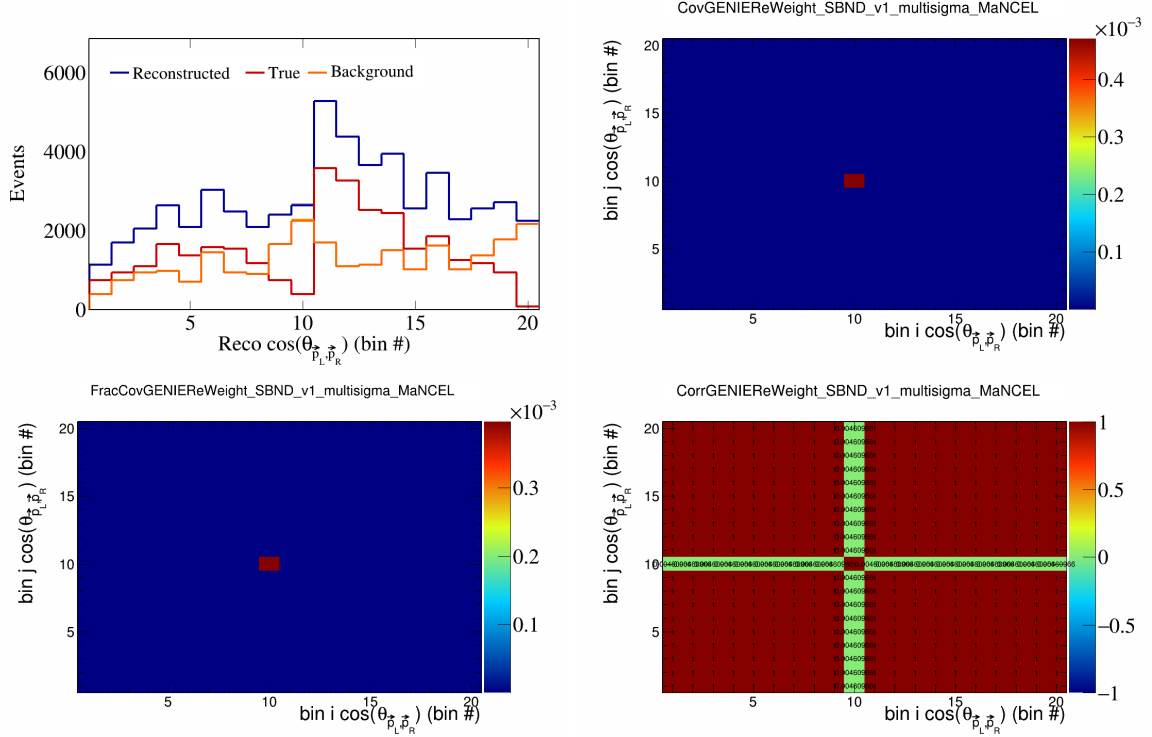


Figure 48: GenieMaNCEL variations for  $\cos(\theta_{\vec{p}_L, \vec{p}_R})$  in  $\cos(\theta_{\vec{p}_\mu})$ .

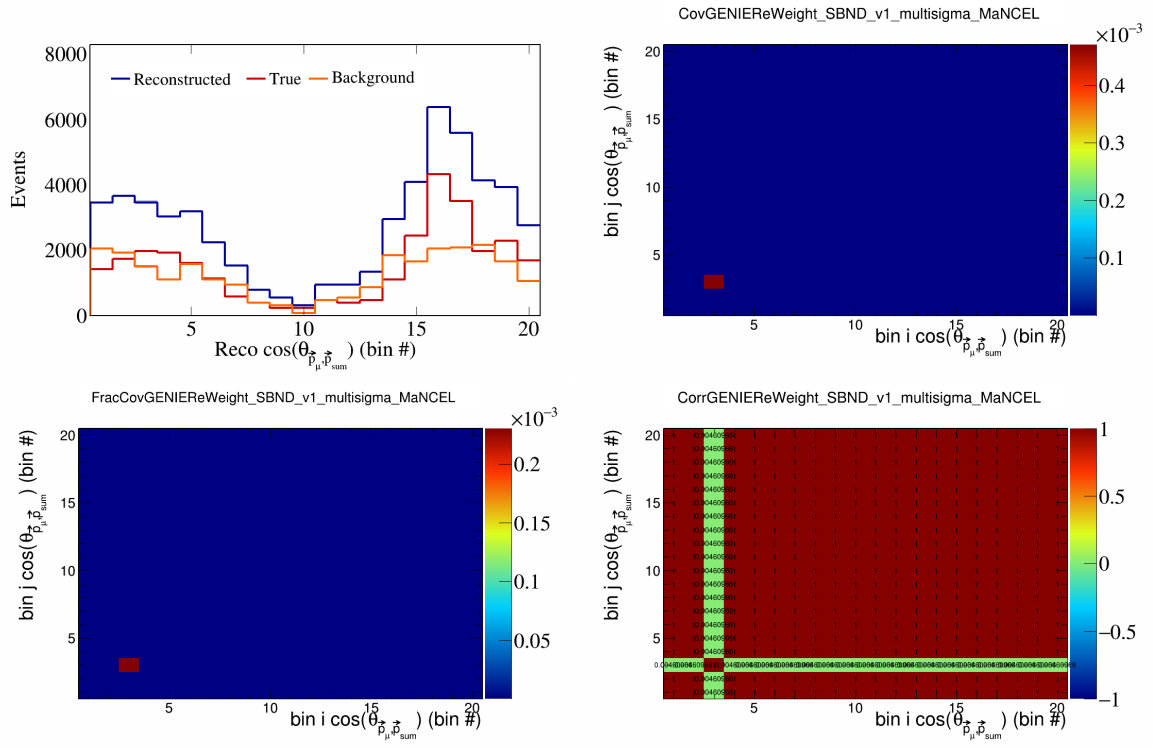


Figure 49: GenieMaNCEL variations for  $\cos(\theta_{\vec{p}_\mu, \vec{p}_{\text{sum}}})$  in  $\cos(\theta_{\vec{p}_\mu})$ .

196 **7 References**

- 197 [1] R. Acciarri, C. Adams, J. Asaadi, B. Baller, T. Bolton, C. Bromberg, F. Cavanna, E. Church, D. Edmunds, A. Ereditato, S. Farooq, B. Fleming, H. Greenlee, G. Horton-Smith, C. James, E. Klein, K. Lang, P. Laurens, R. Mehdiyev, B. Page, O. Palamara, K. Partyka, G. Rameika, B. Rebel, M. Soderberg, J. Spitz, A. M. Szelc, M. Weber, T. Yang, and G. P. Zeller. Detection of back-to-back proton pairs in charged-current neutrino interactions with the argoneut detector in the numi low energy beam line. *Phys. Rev. D*, 90:012008, Jul 2014.
- 203 [2] C. Andreopoulos, A. Bell, D. Bhattacharya, F. Cavanna, J. Dobson, S. Dytman, H. Gallagher, P. Guzowski, R. Hatcher, P. Kehayias, A. Meregaglia, D. Naples, G. Pearce, A. Rubbia, M. Whalley, and T. Yang. The genie neutrino monte carlo generator. *Nuclear Instruments and Methods in Physics Research Section A: Accelerators, Spectrometers, Detectors and Associated Equipment*, 614(1):87–104, 2010.
- 208 [3] Costas Andreopoulos, Christopher Barry, Steve Dytman, Hugh Gallagher, Tomasz Golan, Robert Hatcher, Gabriel Perdue, and Julia Yarba. The genie neutrino monte carlo generator: Physics and user manual, 2015.
- 211 [4] D. Ashery, I. Navon, G. Azuelos, H. K. Walter, H. J. Pfeiffer, and F. W. Schlepütz. True absorption and scattering of pions on nuclei. *Phys. Rev. C*, 23:2173–2185, May 1981.
- 213 [5] P. S. Auchincloss, R. Blair, C. Haber, E. Oltman, W. C. Leung, M. Ruiz, S. R. Mishra, P. Z. Quintas, F. J. Sciulli, M. H. Shaevitz, W. H. Smith, F. S. Merritt, M. Oreglia, P. Reutens, R. Coleman, H. E. Fisk, D. Levinthal, D. D. Yovanovitch, W. Marsh, P. A. Rapidis, H. B. White, A. Bodek, F. Borcherding, N. Giokaris, K. Lang, and I. E. Stockdale. Measurement of the inclusive charged-current cross section for neutrino and antineutrino scattering on isoscalar nucleons. *Zeitschrift für Physik C Particles and Fields*, 48(3):411–431, Sep 1990.
- 219 [6] Ch. Berger and L. M. Sehgal. Lepton mass effects in single pion production by neutrinos. *Phys. Rev. D*, 76:113004, Dec 2007.
- 221 [7] Ch. Berger and L. M. Sehgal. Partially conserved axial vector current and coherent pion production by low energy neutrinos. *Phys. Rev. D*, 79:053003, Mar 2009.
- 223 [8] B. Bourguille, J. Nieves, and F. Sánchez. Inclusive and exclusive neutrino-nucleus cross sections and the reconstruction of the interaction kinematics. *Journal of High Energy Physics*, 2021(4):4, Apr 2021.
- 225 [9] R.C. Carrasco and E. Oset. Interaction of real photons with nuclei from 100 to 500 mev. *Nuclear Physics A*, 536(3):445–508, 1992.
- 227 [10] R. Cruz-Torres, D. Lonardoni, R. Weiss, N. Barnea, D. W. Higinbotham, E. Piasetzky, A. Schmidt, L. B. Weinstein, R. B. Wiringa, and O. Hen. Many-body factorization and position-momentum equivalence of nuclear short-range correlations. *Nature Phys.*, 17(3):306–310, 2021.
- 230 [11] Jonathan Engel. Approximate treatment of lepton distortion in charged-current neutrino scattering from nuclei. *Phys. Rev. C*, 57:2004–2009, Apr 1998.
- 232 [12] T. Golan, J.T. Sobczyk, and J. Źmuda. Nuwro: the wrocław monte carlo generator of neutrino interactions. *Nuclear Physics B - Proceedings Supplements*, 229-232:499, 2012. Neutrino 2010.
- 234 [13] Krzysztof M. Graczyk and Jan T. Sobczyk. Form factors in the quark resonance model. *Phys. Rev. D*, 77:053001, Mar 2008.
- 236 [14] Yoshinari Hayato and Luke Pickering. The neut neutrino interaction simulation program library. *The European Physical Journal Special Topics*, 230(24):4469–4481, Dec 2021.
- 238 [15] Teppei Katori. Meson exchange current (MEC) models in neutrino interaction generators. *AIP Conference Proceedings*, 1663(1):030001, 05 2015.

- 240 [16] Konstantin S. Kuzmin, Vladimir V. Lyubushkin, and Vadim A. Naumov. Lepton polarization in neu-  
241 trino–nucleon interactions. *Modern Physics Letters A*, 19(38):2815–2829, 2004.
- 242 [17] T. Leitner, L. Alvarez-Ruso, and U. Mosel. Charged current neutrino-nucleus interactions at interme-  
243 diate energies. *Phys. Rev. C*, 73:065502, Jun 2006.
- 244 [18] C.H. Llewellyn Smith. Neutrino reactions at accelerator energies. *Physics Reports*, 3(5):261–379, 1972.
- 245 [19] Selection of numu charged current induced interactions with  $N > 0$  protons and performance of events  
246 with  $N = 2$  protons in the final state in the MicroBooNE detector from the BNB, Oct 2018.
- 247 [20] First Extraction of Single Differential Cross-Sections on Argon for CC1 $\mu$ 2p0 $\pi$  Event Topologies in the  
248 MicroBooNE Detector. May 2022.
- 249 [21] Ulrich Mosel. Neutrino event generators: foundation, status and future. *Journal of Physics G: Nuclear  
250 and Particle Physics*, 46(11):113001, Sep 2019.
- 251 [22] J. Nieves, J. E. Amaro, and M. Valverde. Inclusive quasielastic charged-current neutrino-nucleus reac-  
252 tions. *Phys. Rev. C*, 70:055503, Nov 2004.
- 253 [23] J. Nieves, F. Sánchez, I. Ruiz Simo, and M. J. Vicente Vacas. Neutrino energy reconstruction and the  
254 shape of the charged current quasielastic-like total cross section. *Phys. Rev. D*, 85:113008, Jun 2012.
- 255 [24] J. Nieves, I. Ruiz Simo, and M. J. Vicente Vacas. Inclusive charged-current neutrino-nucleus reactions.  
256 *Phys. Rev. C*, 83:045501, Apr 2011.
- 257 [25] J. Schwehr, D. Cherdack, and R. Gran. Genie implementation of ific valencia model for qe-like 2p2h  
258 neutrino-nucleus cross section, 2017.
- 259 [26] Torbjörn Sjöstrand, Stephen Mrenna, and Peter Skands. Pythia 6.4 physics and manual. *Journal of  
260 High Energy Physics*, 2006(05):026, may 2006.
- 261 [27] Júlia Tena-Vidal, Costas Andreopoulos, Adi Ashkenazi, Christopher Barry, Steve Dennis, Steve Dyt-  
262 man, Hugh Gallagher, Steven Gardiner, Walter Giele, Robert Hatcher, Or Hen, Libo Jiang, Igor D.  
263 Kakorin, Konstantin S. Kuzmin, Anselmo Meregaglia, Vadim A. Naumov, Afroditi Papadopoulou,  
264 Gabriel Perdue, Marco Roda, Vladyslav Syrotenko, and Jeremy Wolcott. Neutrino-nucleon cross-section  
265 model tuning in genie v3. *Phys. Rev. D*, 104:072009, Oct 2021.
- 266 [28] U. K. Yang and A. Bodek. Parton distributions,  $d/u$ , and higher twist effects at high  $x$ . *Phys. Rev.  
267 Lett.*, 82:2467–2470, Mar 1999.